

# Gate-defined topological Josephson junctions in Bernal bilayer graphene

Ying-Ming Xie,<sup>1,2,3</sup> Étienne Lantagne-Hurtubise,<sup>2,3</sup> Andrea F. Young,<sup>4</sup> Stevan Nadj-Perge,<sup>5,3</sup> and Jason Alicea<sup>2,3</sup>

<sup>1</sup>*Department of Physics, Hong Kong University of Science and Technology, Clear Water Bay, Hong Kong, China*

<sup>2</sup>*Department of Physics, California Institute of Technology, Pasadena, California 91125, USA*

<sup>3</sup>*Institute for Quantum Information and Matter,*

*California Institute of Technology, Pasadena CA 91125, USA*

<sup>4</sup>*Department of Physics, University of California at Santa Barbara, Santa Barbara CA 93106, USA*

<sup>5</sup>*T. J. Watson Laboratory of Applied Physics, California Institute of Technology,  
1200 East California Boulevard, Pasadena, California 91125, USA*

(Dated: December 14, 2023)

Recent experiments on Bernal bilayer graphene (BLG) deposited on monolayer WSe<sub>2</sub> revealed robust, ultra-clean superconductivity coexisting with sizable induced spin-orbit coupling. Here we propose BLG/WSe<sub>2</sub> as a platform to engineer *gate-defined* planar topological Josephson junctions, where the normal and superconducting regions descend from a common material. More precisely, we show that if superconductivity in BLG/WSe<sub>2</sub> is gapped and emerges from a parent state with intervalley coherence, then MZMs can form in the barrier region upon applying weak in-plane magnetic fields. Our results spotlight a potential pathway for ‘internally engineered’ topological superconductivity that minimizes detrimental disorder and orbital-magnetic-field effects.

Experimental searches for non-Abelian anyons have to date largely followed two complementary paths. The first seeks intrinsic realizations of strongly correlated topological phases of matter, most notably non-Abelian fractional quantum Hall states [1] and quantum spin liquids [2]. The second endeavors to engineer topological superconductors by interfacing well-understood building blocks—e.g., conventional superconductors and semiconductors—that originate from disparate materials [3–18]. One can, however, contemplate a middle ground between these strategies, wherein phases of matter intrinsic to a *single medium* are leveraged to ‘internally engineer’ topological superconductivity. Graphene multilayers comprise an attractive platform for the latter approach given their extraordinarily rich and tunable phase diagrams. As proof of concept, Ref. 19 proposed that gate-defined wires judiciously immersed between gapped phases of twisted bilayer graphene [20–24], or its multilayer generalizations [25–29], could realize topological superconductivity without invoking ‘external’ proximity effects (see also Refs. 30–33 for related architectures).

*Untwisted* (i.e., crystalline) graphene multilayers exhibit phase diagrams whose richness and tunability rival that of their twisted counterparts. Here, applying a perpendicular displacement field  $D$  opens a gap at charge neutrality and locally flattens the bands near the Brillouin zone corners—providing a knob to continuously tune the strength of electronic correlations. Experiments have reported a series of correlation-driven symmetry-broken metallic states together with superconductivity in both Bernal bilayer graphene (BLG) [34–39] and rhombohedral trilayer graphene [40, 41], inspiring various theory proposals for the underlying pairing mechanism [42–58]. In BLG, superconductivity was first observed over a narrow density window in the presence of in-plane magnetic fields  $B_{\parallel} \gtrsim 150$  mT, with a low critical temperature  $T_c \approx 30$  mK [34]. More recent experiments [37, 38] found that placing BLG adjacent to monolayer WSe<sub>2</sub> both gen-

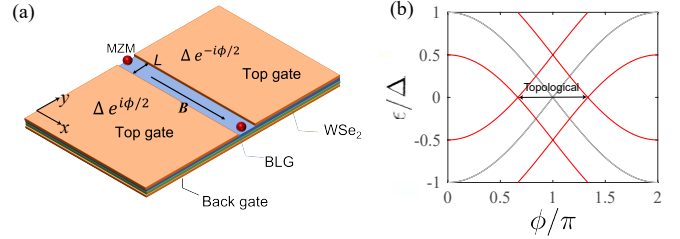


FIG. 1. (a) Gate-defined Josephson junction in BLG/WSe<sub>2</sub> predicted to host Majorana zero-energy modes (MZMs) near a phase difference  $\phi = \pi$  with small in-plane magnetic fields  $\mathbf{B}$ . (b) Andreev bound states spectrum from Eq. (8) with Zeeman energy  $\hbar = 0$  (gray) and  $\hbar = 0.5\Delta$  (red), the latter opening a topological regime.

erates appreciable spin-orbit coupling (SOC) and promotes Cooper pairing: Superconductivity appears over a broader density window within a symmetry-broken parent metallic phase, with  $T_c$  up to hundreds of mK, and without any applied magnetic field. Similar trends have now been observed in several graphene-based systems [23, 37, 59], suggesting a deep connection between SOC and enhanced pairing [50–52, 60].

Here we propose BLG/WSe<sub>2</sub> as a new platform for internally engineered topological superconductivity. Our proposal is inspired by seminal theory works [61, 62] which showed that spin-orbit-coupled planar Josephson junctions at a phase difference of  $\pi$  can in principle host topological superconductivity at arbitrarily weak magnetic fields. Numerous experiments have since pursued this approach in junctions fashioned from proximitized heterostructures [63–67]. We show that Josephson junctions *generated solely by electrostatic gating* in BLG/WSe<sub>2</sub> [Fig. 1(a)] can similarly host a topological regime at weak magnetic fields, provided two requirements are satisfied: Superconductivity native to

BLG/WSe<sub>2</sub> must exhibit a bulk gap (to ensure well-defined Andreev bound states (ABSs) in the junction) and descend from a symmetry-broken normal state with intervalley coherence (to lift valley degeneracy while maintaining the resonance condition for intervalley Cooper pairing). At present the superconducting order parameter and normal-state symmetry in BLG/WSe<sub>2</sub> remain unknown. Hartree-Fock treatments do, however, predict that various types of IVC states are energetically competitive in BLG [37, 60], rhombohedral trilayer graphene [43, 68–70], and twisted bilayer graphene [71–74] (see also a recent tensor-network study [75]). Moreover, IVC order was recently imaged using STM in monolayer graphene in its zeroth Landau level [76, 77] as well as in twisted graphene bilayers [78] and trilayers [79]. Turning the problem on its head, one can view our proposal as a transport probe of IVC order in BLG/WSe<sub>2</sub>.

Aside from eliminating the need for heterostructure engineering, our proposal entails two other key advantages: (1) Superconductivity in BLG/WSe<sub>2</sub> occurs deep in the clean limit [34, 37], thereby mitigating adversarial disorder effects that remain a major obstruction in the pursuit of topological superconductivity and (2) the atomically thin nature of the setup reduces detrimental orbital effects of in-plane magnetic fields [67, 80, 81].

**Symmetry-based low-energy description.** First we derive a minimal effective Hamiltonian for the valence band of BLG/WSe<sub>2</sub> at large displacement fields  $D$ —where superconductivity emerges. As a baseline, Fig. 2(a) sketches the large- $D$  valence band in the absence of SOC. The low-energy degrees of freedom carry spin and valley quantum numbers associated with Pauli matrices  $s_{x,y,z}$  and  $\tau_{x,y,z}$ , respectively. The system preserves time-reversal symmetry  $\mathcal{T} = i\tau_x s_y \mathcal{K}$  ( $\mathcal{K}$  denotes complex conjugation) and three-fold rotations  $C_3 = e^{-i\frac{2\pi}{3}s_z}$ . We also impose the approximate  $x \rightarrow -x$  mirror symmetry  $M_x = i\tau_x s_x$ , even though it is weakly broken by the WSe<sub>2</sub> substrate, and (for now) enforce valley conservation.

We express the single-particle Hamiltonian respecting these symmetries as

$$H_0(\mathbf{k}) = h_0(\mathbf{k}) + h_{\text{so}}(\mathbf{k}), \quad (1)$$

where  $\mathbf{k}$  denotes momentum measured with respect to the  $K$  and  $K'$  points. The first term captures the SOC-free band dispersion and can be decomposed as  $h_0(\mathbf{k}) = \xi_0(\mathbf{k}) + \xi_1(\mathbf{k})\tau_z$ . We take  $\xi_0(\mathbf{k}) \approx -\mu + t_a \mathbf{k}^2 + t_c \mathbf{k}^4$  with  $\mu$  the chemical potential; the valley-dependent contribution encodes trigonal warping and, to leading order in momentum, takes the form  $\xi_1(\mathbf{k}) \approx t_b(k_x^3 - 3k_x k_y^2)$ . By fitting to the full dispersion [82], we estimate  $t_a = 4 \text{ eV} \cdot a^2$ ,  $t_b = -60 \text{ eV} \cdot a^3$ ,  $t_c = -1500 \text{ eV} \cdot a^4$ , with  $a = 0.246 \text{ nm}$  the lattice constant. The second term in Eq. (1) captures SOC in BLG inherited via virtual tunneling to WSe<sub>2</sub>:

$$h_{\text{so}}(\mathbf{k}) = \frac{\beta_I}{2} \tau_z s_z + \alpha_R (k_x s_y - k_y s_x). \quad (2)$$

Here,  $\beta_I$  and  $\alpha_R$  respectively denote Ising and Rashba SOC couplings, whose magnitudes depend on the

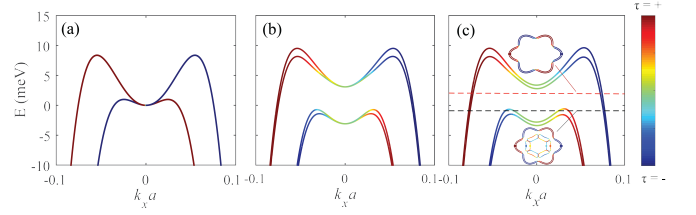


FIG. 2. Valence bands of BLG/WSe<sub>2</sub> at large displacement fields, calculated from Eq. (4) with  $k_y = 0$  and  $\lambda_1 = 0$ . Parameters are (a)  $\beta_I = \alpha_R = \lambda_0 = 0$  and (b,c)  $\beta_I = 1.4 \text{ meV}$ ,  $\alpha_R = 2 \text{ meV} \cdot a$ ,  $\lambda_0 = 3 \text{ meV}$ ; panel (c) further includes a Zeeman field  $h = 0.3 \text{ meV}$  (along the  $x$ -direction). Insets in (c) show the Fermi pockets arising with chemical potentials shown by the red and black dashed lines. Energy bands are colored according to their valley projection.

BLG/WSe<sub>2</sub> interface quality and twist angle [48, 83–85]. For example,  $\beta_I \sim 0.7\text{--}2 \text{ meV}$  was extracted using quantum Hall measurements in different devices [37, 38, 86]. The Rashba scale is harder to directly measure, but can be conservatively estimated [82] as  $\alpha_R \sim 1\text{--}3 \text{ meV} \cdot a$ .

**Intervalley coherence.** Topological superconductivity emerges when an odd number of Fermi surfaces acquire a pairing gap. To this end, SOC in coordination with a Zeeman field facilitates the removal of spin degeneracy, though valley degeneracy in BLG provides an added obstruction. Coulomb interactions can lift the latter degeneracy by promoting symmetry-breaking within the spin-valley subspace, akin to Stoner ferromagnetism [34, 37, 40]. Valley polarized states—in which electrons preferentially populate either the  $K$  or  $K'$  valley—are antagonistic to Cooper pairing and thus likely irrelevant for the parent state of superconductivity. We instead focus on IVC orders, wherein valley degeneracy is lifted via spontaneous coherent tunneling between  $K$  and  $K'$ ; such states more naturally host superconductivity since the resonance condition for intervalley Cooper pairing can persist. Table I in the SM [82] classifies possible IVC orders. While we expect that our proposal holds for generic IVC states, so long as they support gapped zero-momentum Cooper pairing, we focus for concreteness on the subset that preserves  $\mathcal{T}$ ,  $C_3$ , and  $M_x$ . To linear order in momentum, the corresponding IVC order parameter can be expressed as

$$\Delta_{\text{IVC}}(\mathbf{k}) = \lambda_0 \tau_x + \lambda_1 \tau_x (k_x s_y - k_y s_x), \quad (3)$$

where  $\lambda_0$  describes a spin- and momentum-independent contribution and  $\lambda_1$  encodes a spin-valley-orbit coupling.

Supplementing Eq. (1) with both the above IVC order parameter and an in-plane Zeeman field  $\mathbf{h}$  yields the putative normal-state Hamiltonian

$$H(\mathbf{k}) = H_0(\mathbf{k}) + \Delta_{\text{IVC}}(\mathbf{k}) + \mathbf{h} \cdot \mathbf{s} \quad (4)$$

that can exhibit fully lifted spin and valley degeneracies. Figure 2(b,c) sketches the band structure evolution upon (b) turning on SOC and IVC order and then (c) further adding a Zeeman field.

When the chemical potential intersects only the upper pair of bands [red dashed line in Fig. 2(c)], one can further distill the model by projecting out the lower, inert bands—yielding an effective Hamiltonian

$$\tilde{H}(\mathbf{k}) = \xi_0(\mathbf{k}) + \tilde{\beta}_I(k_x^3 - 3k_x k_y^2)\sigma_z + \tilde{\alpha}_R(k_x\sigma_y - k_y\sigma_x) + \tilde{h} \cdot \boldsymbol{\sigma} \quad (5)$$

valid in the regime  $h \ll \sqrt{\lambda_0^2 + \frac{\beta_I^2}{4}}$ . Here  $\sigma_{x,y,z}$  are Pauli matrices acting in the low-energy subspace and

$$\tilde{\beta}_I = \frac{t_b\beta_I}{2\sqrt{\lambda_0^2 + \frac{\beta_I^2}{4}}}, \quad \tilde{\alpha}_R = \frac{\alpha_R\lambda_0}{\sqrt{\lambda_0^2 + \frac{\beta_I^2}{4}}} + \lambda_1, \quad \tilde{h} = \frac{h\lambda_0}{\sqrt{\lambda_0^2 + \frac{\beta_I^2}{4}}}. \quad (6)$$

Equation (5) represents a two-band model for fermions with cubic-in-momentum Ising SOC and linear-in-momentum Rashba SOC. Note that IVC order suppresses  $\tilde{\beta}_I$ , but enhances  $\tilde{\alpha}_R$  and  $\tilde{h}$  through a linear coupling to the bare Zeeman field  $h$  and Rashba SOC  $\alpha_R$ , which would only be quadratic when  $\lambda_0 = 0$ . The spin-valley-orbit term  $\lambda_1$  simply contributes to the effective Rashba coupling; we thus set  $\lambda_1 = 0$  hereafter. Parameter renormalizations in Eq. (6) may be relevant for the unconventional Pauli-limit-violation trends observed in Ref. 37.

**Topological Josephson junctions.** We now incorporate superconductivity, assuming for simplicity an s-wave order parameter—though we stress that our scheme readily extends to more exotic pairings provided they generate a bulk gap. The corresponding Bogoliubov-de Gennes (BdG) Hamiltonian reads

$$\tilde{H}_{\text{BdG}}(\mathbf{k}) = \begin{pmatrix} \tilde{H}(\mathbf{k}) & i\Delta\sigma_y \\ -i\Delta\sigma_y & -\tilde{H}^*(-\mathbf{k}) \end{pmatrix} \quad (7)$$

with  $\Delta$  the pairing amplitude. To set the stage, we first consider a simple case where  $\xi_0(\mathbf{k}) \approx -\mathbf{k}^2/2m - \mu$  and  $\tilde{\beta}_I k_F^3 \ll \tilde{\alpha}_R k_F$  ( $m$  is an effective mass and  $k_F$  is the Fermi momentum). Equation (7) then maps to the Hamiltonian for a proximitized Rashba-coupled 2D electron gas under in-plane magnetic fields—exactly the ingredients required to create topological superconductivity in planar Josephson junctions [61, 62].

Next we consider a Josephson junction, with phase difference  $\phi$ , formed by gate-tuning a barrier region of length  $L$  into a normal phase with  $\Delta = 0$ . The magnetic field is oriented parallel to the junction (along the  $x$  direction), which is optimal for accessing the topological regime [61, 62]. Within the barrier the relevant Fermi velocity  $v_F$  arises from the large pockets in Fig. 2(c); band-structure estimates give  $v_F \sim 5 \times 10^5$  m/s. For reasonable junction lengths  $L \sim 50 - 200$  nm, the corresponding Thouless energy  $E_T = \frac{\pi v_F}{2L} \sim 0.8 - 3$  meV greatly exceeds both the pairing energy  $\Delta$  and renormalized Zeeman energy  $\tilde{h}$ . We therefore assume the short-junction limit  $E_T \gg \Delta, \tilde{h}$  below.

Topological phase transitions are determined by computing the ABS spectrum at  $k_x = 0$  using the standard scattering matrix method (for details see SM). In the absence of normal reflections at the interfaces, the  $k_x = 0$

ABS energies take the simple form

$$\epsilon_{\pm,\eta}(\phi) = \eta\tilde{h} \pm \Delta \cos(\phi/2), \quad (8)$$

where  $\eta = \pm$  is a pseudospin label. Figure 1(b) plots these energies at  $\tilde{h} = 0$  and  $\tilde{h} = 0.5\Delta$ . In the zero-field limit, both  $\eta = \pm$  branches become gapless at a phase difference  $\phi = \pi$ . Turning on the in-plane Zeeman field shifts the gap closing points to  $\phi \neq \pi$ , thereby opening up a topological regime. The above features are consistent with the results of Refs. [61, 62], except that we consider a uniform Zeeman energy in the barrier and superconducting regions. The  $\tilde{h}$  contribution in  $\epsilon_{\pm,\eta}$  descends from the Zeeman energy in the superconductors—which produces non-degenerate  $k_x = 0$  energies at  $\phi = 0$ .

**Numerical phase diagram.** We now verify the above physical picture via a numerical calculation of the ABSs in a more realistic BLG/WSe<sub>2</sub> model. We rewrite the four-band Hamiltonian capturing the low-energy bands, Eqs. (4) and (7), as a tight-binding model in the  $y$  direction for a given  $k_x$  (see SM Sec. V). To emulate experiments, where quantum oscillations reveal that superconductivity occurs in a regime with both large and small pockets [37], we fix the chemical potential in the superconducting regions to  $\mu_2 = -1$  meV [black dashed line in Fig. 2(c)]. The chemical potential  $\mu_1$  in the barrier can be tuned independently, including to a regime with only large pockets (where the effective two-band model applies). For concreteness, unless specified otherwise we set  $\mu_1 = 2$  meV,  $\beta_I = 1.4$  meV,  $\alpha_R = 2$  meV·Å,  $\lambda_0 = 3$  meV,  $\lambda_1 = 0$ , and  $\Delta = 0.1$  meV; under BCS weak-coupling assumptions the latter corresponds to  $T_c \sim 600$  mK. Note that this choice of  $\lambda_0$  and  $\beta_I$  gives  $\tilde{h} \approx h$ .

The ABS spectrum follows by diagonalizing the 1D tight-binding model for each  $k_x$ . Figure 3(a,b) presents the  $k_x = 0$  energies versus  $\phi$  for (a)  $h = 0$  and (b)  $h = 0.5\Delta$ . In (a), lifting of valley degeneracy by IVC order leaves two nearly degenerate ABSs with a small splitting (away from  $\phi = 0, \pi$ ). Panel (b) shows that a Zeeman field nucleates a topological region centered around  $\phi = \pi$ , separated from the trivial regions by a  $k_x = 0$  gap closure. These observations agree well with simpler two-band-model results from Fig. 1(b); indeed the bound states continue to be well-captured by Eq. (8) [see dashed lines in Fig. 3(b)]. Figure 3(c) shows the broader phase diagram, obtained from the  $k_x = 0$  gap ( $E_g$ ) illustrated by the colormap, versus  $h/\Delta$  and  $\phi$ . In the topological phase, the minimal gap  $E_{g,m}$  typically appears at finite  $k_x$  and is maximized when SOC effects are dominated by the effective Rashba contribution (see SM Sec. VI). The topological phase transition lines closely emulate the curves  $\tilde{h} = \Delta|\cos(\phi/2)|$  predicted by Eq. (8). For the  $\pi$ -junction, topological superconductivity sets in at arbitrarily weak Zeeman fields—though more generally normal reflections at the interfaces push the required Zeeman field to a finite value (see SM Sec. III) [61]. As the in-plane field increases, the topological phase persists until the superconducting regions become gapless, roughly when the renormalized Zeeman energy  $\tilde{h} \sim \Delta$ .



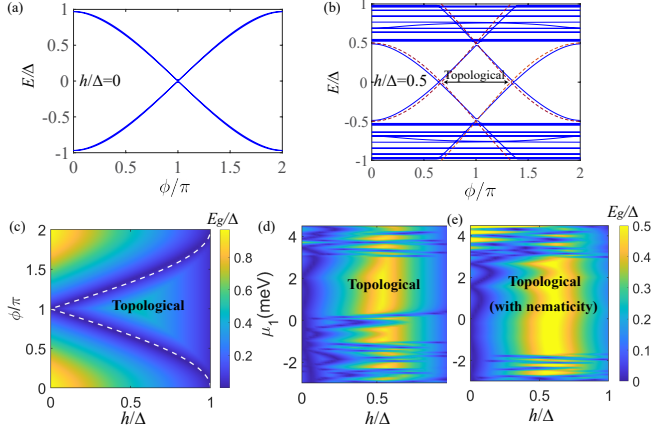


FIG. 3. (a,b) ABS energies  $E$  at  $k_x = 0$  as a function of  $\phi$ , obtained from a realistic tight-binding model with Zeeman energy (a)  $h = 0$  and (b)  $h = 0.5\Delta$ . Dashed lines in (b) trace the analytical result Eq. (8) obtained in the short junction limit. (c-e) Phase diagrams as a function of (c)  $h, \phi$  and (d,e)  $h, \mu_1$ . In (c) the dashed white line indicates  $h = \Delta|\cos(\phi/2)|$ , which roughly captures the topological phase boundary. Panel (e) is the same as (d), but with nematicity phenomenologically incorporated. Data correspond to  $L = 158$  nm and  $\phi = \pi$ .

Figure 3(d) reveals the dependence of  $E_g$  on  $h/\Delta$  and the barrier chemical potential  $\mu_1$  at  $\phi = \pi$ . A robust topological region occurs for  $\mu_1 \sim 0 - 3$  meV, where the barrier hosts only two large hole pockets. Outside of this range, additional small pockets arise—see Fig. 2(c)—that engender frequent topological phase transitions. Quantum oscillations, however, indicate that the number of small pockets above  $T_c$  is smaller than the six naively predicted by band theory [37], which was suggested to arise from electronic nematicity [87, 88]. Including nematicity in our calculation (see SM Sec. IV), we find that the overall features of the phase diagram persist, while the extent of the robust topological region increases due to fewer “polluting” low-energy states.

**Atomically resolved MZM wavefunctions.** Topological superconductivity acquires a novel fingerprint in our setup: The essential ingredient of IVC order generates atomic-scale translation symmetry breaking with an enlarged  $\sqrt{3} \times \sqrt{3}$  Kekulé supercell, which manifests directly in the MZM wavefunctions. Figure 4(a) illustrates the atomically resolved MZM density of states in the barrier (see SM [82] Sec. VIII); the usual exponential localization and Friedel-like oscillations are evident on the scale shown. Fourier transforming the data reveals characteristic momentum-space peaks [Fig. 4(b)] associated with the Kekulé supercell, while Fig. 4(c) zooms in on the red rectangular region from (a) and clearly shows the corresponding atomic-scale ordering. Contrary to the familiar ‘bond-centered’ Kekulé patterns observed in monolayer graphene [76, 77], here symmetry breaking manifests primarily on sites due to sublattice and layer polarization generated at large  $D$  fields. Figure 4(d,e) explores different Kekulé angles  $\theta$ , obtained

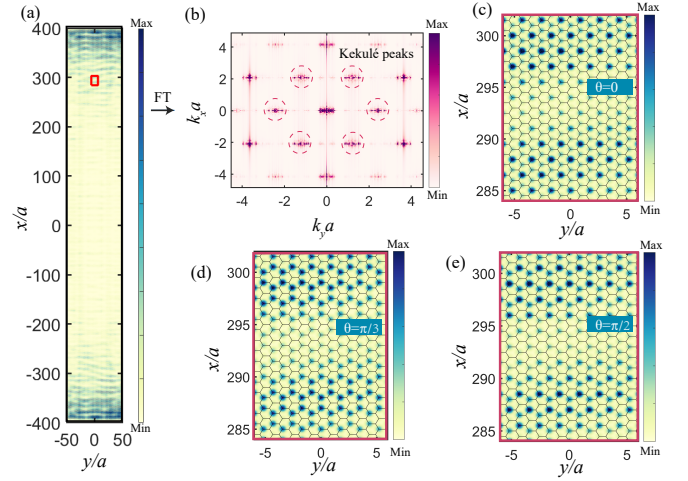


FIG. 4. (a) Atomically resolved density of states for the MZM wavefunction in the junction, assuming Kekulé angle  $\theta = 0$ . (b) Fourier transform (FT) of the data in (a) revealing Kekulé peaks resulting from IVC-induced atomic-scale reconstruction. (c-e) Zoom-in of the red rectangular region in (a) showing the evolution of the symmetry-breaking pattern with different Kekulé angles. Data correspond to  $L = 160$  a,  $h/\Delta = 0.8$  and  $\phi = \pi$ .

by replacing the  $\tau_x$  order parameter considered thus far with  $\cos(\theta)\tau_x + \sin(\theta)\tau_y$ . The resulting Kekulé pattern intimately relates to  $\theta$ , allowing experimental characterization of IVC order via the MZMs.

STM measurements that resolve zero-bias peaks without the atomic-scale structure predicted here could arise from trivial ABSs originating from disorder [89–91] or inhomogeneities near the barrier ends [92–94] (see Refs. [18, 95] for reviews). Conversely, and more definitively, observing localized zero modes at both junction ends that appear near  $\phi = \pi$  and exhibit Kekulé order would strongly support topological superconductivity arising from an IVC normal state.

**Discussion and Outlook.** We proposed a route to one-dimensional topological superconductivity where all required ingredients—SOC, Cooper pairing, and the ability to fabricate planar Josephson junctions—appear natively in a *single* BLG/WSe<sub>2</sub> platform. Our proposal relies on two reasonable but so far untested assumptions: a gapped superconducting phase and a normal parent state with intervalley coherence. The ultra-clean nature of superconductivity in BLG [34, 37], with an electronic mean-free path far exceeding the coherence length, presents an enormous virtue that potentially circumvents disorder effects that plague proximitized nanowires [89–91] and Josephson junctions [63, 64, 67]. Weak disorder arising, e.g., from imperfections in the geometry of gates defining the junction, can even enhance the robustness of the topological phase by decreasing the Majorana localization length [96]. A more controllable route to the same goal consists of gate-defining the junction in a zigzag geometry designed to enhance Andreev reflections [97].



Our proposal readily generalizes to more exotic order parameters (see SM Table I). If either the normal or superconducting state spontaneously breaks time-reversal symmetry, topological superconductivity could arise without an applied magnetic field [19]. For example, a spin-nematic IVC state described by a  $\tau_x s_x$  order parameter generates an effective Zeeman field when projected to the low-energy subspace of Eq. (5). We also expect our proposal to be relevant for a broader family of graphene-based structures. Substantial efforts have been devoted to gate-defined wires and Josephson junctions in twisted bilayer graphene [19, 30–33, 98–100], which also enjoys exquisite gate tunability but suffers from more prevalent disorder [101, 102]. Rhombohedral trilayer graphene offers a cleaner platform for gate-tunable correlated states and superconductivity [40, 41]—thus presenting another interesting medium for future exploration along these lines.

**Acknowledgements.** We are grateful to An-

drey Antipov, Cory Dean, Cyprian Lewandowski, Alex Thomson, and Yiran Zhang for enlightening discussions. Y.M.X. acknowledges the support of HKRGC through PDFS2223-6S01. E.L.-H. was supported by the Gordon and Betty Moore Foundation’s EPiQS Initiative, Grant GBMF8682. J.A. was supported by the Army Research Office under Grant Award W911NF-17-1-0323; the Caltech Institute for Quantum Information and Matter, an NSF Physics Frontiers Center with support of the Gordon and Betty Moore Foundation through Grant GBMF1250; and the Walter Burke Institute for Theoretical Physics at Caltech. The U.S. Department of Energy, Office of Science, National Quantum Information Science Research Centers, Quantum Science Center supported the symmetry-based analysis of this work. S.N.P. acknowledges support of Office of Naval Research (grant no. N142112635) and NSF-CAREER (DMR-1753306) programs. Work at UCSB was supported by the U.S. Department of Energy (Award No. DE-SC0020305).

- 
- [1] C. Nayak, S. H. Simon, A. Stern, M. Freedman, and S. Das Sarma, Non-abelian anyons and topological quantum computation, *Rev. Mod. Phys.* **80**, 1083 (2008).
  - [2] A. Kitaev, Anyons in an exactly solved model and beyond, *Annals of Physics* **321**, 2 (2006).
  - [3] L. Fu and C. L. Kane, Superconducting proximity effect and majorana fermions at the surface of a topological insulator, *Phys. Rev. Lett.* **100**, 096407 (2008).
  - [4] J. D. Sau, R. M. Lutchyn, S. Tewari, and S. Das Sarma, Generic new platform for topological quantum computation using semiconductor heterostructures, *Phys. Rev. Lett.* **104**, 040502 (2010).
  - [5] R. M. Lutchyn, J. D. Sau, and S. Das Sarma, Majorana fermions and a topological phase transition in semiconductor-superconductor heterostructures, *Phys. Rev. Lett.* **105**, 077001 (2010).
  - [6] Y. Oreg, G. Refael, and F. von Oppen, Helical liquids and majorana bound states in quantum wires, *Phys. Rev. Lett.* **105**, 177002 (2010).
  - [7] J. Alicea, Majorana fermions in a tunable semiconductor device, *Phys. Rev. B* **81**, 125318 (2010).
  - [8] V. Mourik, K. Zuo, S. M. Frolov, S. R. Plissard, E. P. A. M. Bakkers, and L. P. Kouwenhoven, Signatures of majorana fermions in hybrid superconductor-semiconductor nanowire devices, *Science* **336**, 1003 (2012).
  - [9] T.-P. Choy, J. M. Edge, A. R. Akhmerov, and C. W. J. Beenakker, Majorana fermions emerging from magnetic nanoparticles on a superconductor without spin-orbit coupling, *Phys. Rev. B* **84**, 195442 (2011).
  - [10] S. Nadj-Perge, I. K. Drozdov, B. A. Bernevig, and A. Yazdani, Proposal for realizing majorana fermions in chains of magnetic atoms on a superconductor, *Phys. Rev. B* **88**, 020407 (2013).
  - [11] F. Pientka, L. I. Glazman, and F. von Oppen, Topological superconducting phase in helical shiba chains, *Phys. Rev. B* **88**, 155420 (2013).
  - [12] J. Klinovaja, P. Stano, A. Yazdani, and D. Loss, Topological superconductivity and majorana fermions in rkky systems, *Phys. Rev. Lett.* **111**, 186805 (2013).
  - [13] S. Nadj-Perge, I. K. Drozdov, J. Li, H. Chen, S. Jeon, J. Seo, A. H. MacDonald, B. A. Bernevig, and A. Yazdani, Observation of majorana fermions in ferromagnetic atomic chains on a superconductor, *Science* **346**, 602 (2014).
  - [14] X.-L. Qi and S.-C. Zhang, Topological insulators and superconductors, *Rev. Mod. Phys.* **83**, 1057 (2011).
  - [15] J. Alicea, New directions in the pursuit of majorana fermions in solid state systems, *Rep. Prog. Phys.* **75**, 076501 (2012).
  - [16] C. Beenakker, Search for majorana fermions in superconductors, *Annu. Rev. Condens. Matter Phys.* **4**, 113 (2013).
  - [17] R. M. Lutchyn, E. P. A. M. Bakkers, L. P. Kouwenhoven, P. Krogstrup, C. M. Marcus, and Y. Oreg, Majorana zero modes in superconductor-semiconductor heterostructures, *Nat. Rev. Mater.* **3**, 52 (2018).
  - [18] K. Flensberg, F. von Oppen, and A. Stern, Engineered platforms for topological superconductivity and majorana zero modes, *Nat. Rev. Mater.* **6**, 944 (2021).
  - [19] A. Thomson, I. M. Sorensen, S. Nadj-Perge, and J. Alicea, Gate-defined wires in twisted bilayer graphene: From electrical detection of intervalley coherence to internally engineered majorana modes, *Phys. Rev. B* **105**, L081405 (2022).
  - [20] Y. Cao, V. Fatemi, S. Fang, K. Watanabe, T. Taniguchi, E. Kaxiras, and P. Jarillo-Herrero, Unconventional superconductivity in magic-angle graphene superlattices, *Nature* **556**, 43 (2018).
  - [21] M. Yankowitz, S. Chen, H. Polshyn, Y. Zhang, K. Watanabe, T. Taniguchi, D. Graf, A. F. Young, and C. R. Dean, Tuning superconductivity in twisted bilayer graphene, *Science* **363**, 1059 (2019).
  - [22] X. Lu, P. Stepanov, W. Yang, M. Xie, M. A. Aamir, I. Das, C. Urgell, K. Watanabe, T. Taniguchi, G. Zhang, A. Bachtold, A. H. MacDonald, and D. K. Efetov, Superconductors, orbital magnets and correlated states in

- magic-angle bilayer graphene, *Nature* **574**, 653 (2019).
- [23] H. S. Arora, R. Polski, Y. Zhang, A. Thomson, Y. Choi, H. Kim, Z. Lin, I. Z. Wilson, X. Xu, J.-H. Chu, K. Watanabe, T. Taniguchi, J. Alicea, and S. Nadj-Perge, Superconductivity in metallic twisted bilayer graphene stabilized by  $\text{wse}_2$ , *Nature* **583**, 379 (2020).
- [24] M. Oh, K. P. Nuckolls, D. Wong, R. L. Lee, X. Liu, K. Watanabe, T. Taniguchi, and A. Yazdani, Evidence for unconventional superconductivity in twisted bilayer graphene, *Nature* **600**, 240 (2021).
- [25] J. M. Park, Y. Cao, K. Watanabe, T. Taniguchi, and P. Jarillo-Herrero, Tunable strongly coupled superconductivity in magic-angle twisted trilayer graphene, *Nature* **590**, 249 (2021).
- [26] Z. Hao, A. M. Zimmerman, P. Ledwith, E. Khalaf, D. H. Najafabadi, K. Watanabe, T. Taniguchi, A. Vishwanath, and P. Kim, Electric field tunable superconductivity in alternating-twist magic-angle trilayer graphene, *Science* **371**, 1133 (2021).
- [27] H. Kim, Y. Choi, C. Lewandowski, A. Thomson, Y. Zhang, R. Polski, K. Watanabe, T. Taniguchi, J. Alicea, and S. Nadj-Perge, Evidence for unconventional superconductivity in twisted trilayer graphene, *Nature* **606**, 494 (2022).
- [28] J. M. Park, Y. Cao, L.-Q. Xia, S. Sun, K. Watanabe, T. Taniguchi, and P. Jarillo-Herrero, Robust superconductivity in magic-angle multilayer graphene family, *Nature Materials* **21**, 877 (2022).
- [29] Y. Zhang, R. Polski, C. Lewandowski, A. Thomson, Y. Peng, Y. Choi, H. Kim, K. Watanabe, T. Taniguchi, J. Alicea, F. von Oppen, G. Refael, and S. Nadj-Perge, Promotion of superconductivity in magic-angle graphene multilayers, *Science* **377**, 1538 (2022).
- [30] D. Rodan-Legrain, Y. Cao, J. M. Park, S. C. de la Barrera, M. T. Randeria, K. Watanabe, T. Taniguchi, and P. Jarillo-Herrero, Highly tunable junctions and non-local josephson effect in magic-angle graphene tunnelling devices, *Nat. Nanotechnol.* **16**, 769 (2021).
- [31] F. K. de Vries, E. Portolés, G. Zheng, T. Taniguchi, K. Watanabe, T. Ihn, K. Ensslin, and P. Rickhaus, Gate-defined josephson junctions in magic-angle twisted bilayer graphene, *Nat. Nanotechnol.* **16**, 760 (2021).
- [32] E. Portolés, S. Iwakiri, G. Zheng, P. Rickhaus, T. Taniguchi, K. Watanabe, T. Ihn, K. Ensslin, and F. K. de Vries, A tunable monolithic squid in twisted bilayer graphene, *Nat. Nanotechnol.* **17**, 1159 (2022).
- [33] J. Díez-Mérida, A. Díez-Carlón, S. Y. Yang, Y.-M. Xie, X.-J. Gao, J. Senior, K. Watanabe, T. Taniguchi, X. Lu, A. P. Higginbotham, K. T. Law, and D. K. Efetov, Symmetry-broken josephson junctions and superconducting diodes in magic-angle twisted bilayer graphene, *Nat. Commun.* **14**, 10.1038/s41467-023-38005-7 (2023).
- [34] H. Zhou, L. Holleis, Y. Saito, L. Cohen, W. Huynh, C. L. Patterson, F. Yang, T. Taniguchi, K. Watanabe, and A. F. Young, Isospin magnetism and spin-polarized superconductivity in bernal bilayer graphene, *Science* **375**, 774 (2022).
- [35] S. C. de la Barrera, S. Aronson, Z. Zheng, K. Watanabe, T. Taniguchi, Q. Ma, P. Jarillo-Herrero, and R. Ashoori, Cascade of isospin phase transitions in bernal-stacked bilayer graphene at zero magnetic field, *Nat. Phys.* **18**, 771 (2022).
- [36] A. M. Seiler, F. R. Geisenhof, F. Winterer, K. Watanabe, T. Taniguchi, T. Xu, F. Zhang, and R. T. Weitz, Quantum cascade of correlated phases in trigonally warped bilayer graphene, *Nature* **608**, 298 (2022).
- [37] Y. Zhang, R. Polski, A. Thomson, É. Lantagne-Hurtubise, C. Lewandowski, H. Zhou, K. Watanabe, T. Taniguchi, J. Alicea, and S. Nadj-Perge, Enhanced superconductivity in spin-orbit proximitized bilayer graphene, *Nature* **613**, 268 (2023).
- [38] L. Holleis, C. L. Patterson, Y. Zhang, H. M. Yoo, H. Zhou, T. Taniguchi, K. Watanabe, S. Nadj-Perge, and A. F. Young, Ising superconductivity and nematicity in bernal bilayer graphene with strong spin orbit coupling (2023), [arXiv:2303.00742 \[cond-mat.supr-con\]](https://arxiv.org/abs/2303.00742).
- [39] J.-X. Lin, Y. Wang, N. J. Zhang, K. Watanabe, T. Taniguchi, L. Fu, and J. I. A. Li, Spontaneous momentum polarization and diodicity in bernal bilayer graphene (2023), [arXiv:2302.04261 \[cond-mat.mes-hall\]](https://arxiv.org/abs/2302.04261).
- [40] H. Zhou, T. Xie, A. Ghazaryan, T. Holder, J. R. Ehrets, E. M. Spanton, T. Taniguchi, K. Watanabe, E. Berg, M. Serbyn, and A. F. Young, Half- and quarter-metals in rhombohedral trilayer graphene, *Nature* **598**, 429 (2021).
- [41] H. Zhou, T. Xie, T. Taniguchi, K. Watanabe, and A. F. Young, Superconductivity in rhombohedral trilayer graphene, *Nature* **598**, 434 (2021).
- [42] A. Ghazaryan, T. Holder, M. Serbyn, and E. Berg, Unconventional superconductivity in systems with annular fermi surfaces: Application to rhombohedral trilayer graphene, *Phys. Rev. Lett.* **127**, 247001 (2021).
- [43] S. Chatterjee, T. Wang, E. Berg, and M. P. Zaletel, Inter-valley coherent order and isospin fluctuation mediated superconductivity in rhombohedral trilayer graphene, *Nat. Commun.* **13**, 6013 (2022).
- [44] T. Cea, P. A. Pantaleón, V. o. T. Phong, and F. Guinea, Superconductivity from repulsive interactions in rhombohedral trilayer graphene: A kohn-luttinger-like mechanism, *Phys. Rev. B* **105**, 075432 (2022).
- [45] A. L. Szabó and B. Roy, Metals, fractional metals, and superconductivity in rhombohedral trilayer graphene, *Phys. Rev. B* **105**, L081407 (2022).
- [46] Y.-Z. You and A. Vishwanath, Kohn-luttinger superconductivity and intervalley coherence in rhombohedral trilayer graphene, *Phys. Rev. B* **105**, 134524 (2022).
- [47] Y.-Z. Chou, F. Wu, J. D. Sau, and S. Das Sarma, Acoustic-phonon-mediated superconductivity in moiréless graphene multilayers, *Phys. Rev. B* **106**, 024507 (2022).
- [48] Y.-Z. Chou, F. Wu, and S. Das Sarma, Enhanced superconductivity through virtual tunneling in bernal bilayer graphene coupled to  $\text{wse}_2$ , *Phys. Rev. B* **106**, L180502 (2022).
- [49] A. S. Patri and T. Senthil, Strong correlations in ab-stacked trilayer graphene: Moiré is important, *Phys. Rev. B* **107**, 165122 (2023).
- [50] J. B. Curtis, N. R. Poniatowski, Y. Xie, A. Yacoby, E. Demler, and P. Narang, Stabilizing fluctuating spin-triplet superconductivity in graphene via induced spin-orbit coupling, *Phys. Rev. Lett.* **130**, 196001 (2023).
- [51] G. Wagner, Y. H. Kwan, N. Bultinck, S. H. Simon, and S. A. Parameswaran, Superconductivity from repulsive interactions in bernal-stacked bilayer graphene (2023), [arXiv:2302.00682 \[cond-mat.supr-con\]](https://arxiv.org/abs/2302.00682).
- [52] A. Jimeno-Pozo, H. Sainz-Cruz, T. Cea, P. A. Pantaleón, and F. Guinea, Superconductivity from elec-

- tronic interactions and spin-orbit enhancement in bilayer and trilayer graphene, *Phys. Rev. B* **107**, L161106 (2023).
- [53] W. Qin, C. Huang, T. Wolf, N. Wei, I. Blinov, and A. H. MacDonald, Functional renormalization group study of superconductivity in rhombohedral trilayer graphene, *Phys. Rev. Lett.* **130**, 146001 (2023).
  - [54] D.-C. Lu, T. Wang, S. Chatterjee, and Y.-Z. You, Correlated metals and unconventional superconductivity in rhombohedral trilayer graphene: A renormalization group analysis, *Phys. Rev. B* **106**, 155115 (2022).
  - [55] H. Dai, R. Ma, X. Zhang, T. Guo, and T. Ma, Quantum monte carlo study of superconductivity in rhombohedral trilayer graphene under an electric field, *Phys. Rev. B* **107**, 245106 (2023).
  - [56] Z. Dong, A. V. Chubukov, and L. Levitov, Transformer spin-triplet superconductivity at the onset of isospin order in bilayer graphene, *Phys. Rev. B* **107**, 174512 (2023).
  - [57] G. Shavit and Y. Oreg, Inducing superconductivity in bilayer graphene by alleviation of the stoner blockade, *Phys. Rev. B* **108**, 024510 (2023).
  - [58] Z. Dong, P. A. Lee, and L. S. Levitov, Signatures of cooper pair dynamics and quantum-critical superconductivity in tunable carrier bands (2023), [arXiv:2304.09812 \[cond-mat.supr-con\]](#).
  - [59] R. Su, M. Kuiri, K. Watanabe, T. Taniguchi, and J. Folk, Superconductivity in twisted double bilayer graphene stabilized by  $wse_2$  (2022), [arXiv:2211.16449 \[cond-mat.supr-con\]](#).
  - [60] M. Xie and S. Das Sarma, Flavor symmetry breaking in spin-orbit coupled bilayer graphene, *Phys. Rev. B* **107**, L201119 (2023).
  - [61] F. Pientka, A. Keselman, E. Berg, A. Yacoby, A. Stern, and B. I. Halperin, Topological superconductivity in a planar josephson junction, *Phys. Rev. X* **7**, 021032 (2017).
  - [62] M. Hell, M. Leijnse, and K. Flensberg, Two-dimensional platform for networks of majorana bound states, *Phys. Rev. Lett.* **118**, 107701 (2017).
  - [63] H. Ren, F. Pientka, S. Hart, A. T. Pierce, M. Kosowsky, L. Lunczer, R. Schlereth, B. Scharf, E. M. Hankiewicz, L. W. Molenkamp, B. I. Halperin, and A. Yacoby, Topological superconductivity in a phase-controlled josephson junction, *Nature* **569**, 93 (2019).
  - [64] A. Fornieri, A. M. Whiticar, F. Setiawan, E. Portolés, A. C. C. Drachmann, A. Keselman, S. Gronin, C. Thomas, T. Wang, R. Kallagher, G. C. Gardner, E. Berg, M. J. Manfra, A. Stern, C. M. Marcus, and F. Nichele, Evidence of topological superconductivity in planar josephson junctions, *Nature* **569**, 89 (2019).
  - [65] C. T. Ke, C. M. Moehle, F. K. de Vries, C. Thomas, S. Metti, C. R. Guinn, R. Kallagher, M. Lodari, G. Scappucci, T. Wang, R. E. Diaz, G. C. Gardner, M. J. Manfra, and S. Goswami, Ballistic superconductivity and tunable  $\pi$ -junctions in insb quantum wells, *Nat. Commun.* **10**, 3764 (2019).
  - [66] M. C. Dartiailh, W. Mayer, J. Yuan, K. S. Wickramasinghe, A. Matos-Abiague, I. Žutić, and J. Shabani, Phase signature of topological transition in josephson junctions, *Phys. Rev. Lett.* **126**, 036802 (2021).
  - [67] A. Banerjee, O. Lesser, M. A. Rahman, H.-R. Wang, M.-R. Li, A. Kringhøj, A. M. Whiticar, A. C. C. Drachmann, C. Thomas, T. Wang, M. J. Manfra, E. Berg, Y. Oreg, A. Stern, and C. M. Marcus, Signatures of a topological phase transition in a planar josephson junction, *Phys. Rev. B* **107**, 245304 (2023).
  - [68] T. Wang, M. Vila, M. P. Zaletel, and S. Chatterjee, Electrical control of magnetism in spin-orbit coupled graphene multilayers (2023), [arXiv:2303.04855 \[cond-mat.str-el\]](#).
  - [69] Y. Zhumagulov, D. Kochan, and J. Fabian, Emergent correlated phases in rhombohedral trilayer graphene induced by proximity spin-orbit and exchange coupling (2023), [arXiv:2305.14277 \[cond-mat.str-el\]](#).
  - [70] J. M. Koh, J. Alicea, and Étienne Lantagne-Hurtubise, Correlated phases in spin-orbit-coupled rhombohedral trilayer graphene (2023), [arXiv:2306.12486 \[cond-mat.str-el\]](#).
  - [71] N. Bultinck, E. Khalaf, S. Liu, S. Chatterjee, A. Vishwanath, and M. P. Zaletel, Ground state and hidden symmetry of magic-angle graphene at even integer filling, *Phys. Rev. X* **10**, 031034 (2020).
  - [72] Y. Zhang, K. Jiang, Z. Wang, and F. Zhang, Correlated insulating phases of twisted bilayer graphene at commensurate filling fractions: A hartree-fock study, *Phys. Rev. B* **102**, 035136 (2020).
  - [73] B. Lian, Z.-D. Song, N. Regnault, D. K. Efetov, A. Yazdani, and B. A. Bernevig, Twisted bilayer graphene. iv. exact insulator ground states and phase diagram, *Phys. Rev. B* **103**, 205414 (2021).
  - [74] G. Wagner, Y. H. Kwan, N. Bultinck, S. H. Simon, and S. A. Parameswaran, Global phase diagram of the normal state of twisted bilayer graphene, *Phys. Rev. Lett.* **128**, 156401 (2022).
  - [75] T. Wang, D. E. Parker, T. Soejima, J. Hauschild, S. Anand, N. Bultinck, and M. P. Zaletel, Kekulé spiral order in magic-angle graphene: a density matrix renormalization group study (2022), [arXiv:2211.02693 \[cond-mat.str-el\]](#).
  - [76] X. Liu, G. Farahi, C.-L. Chiu, Z. Papic, K. Watanabe, T. Taniguchi, M. P. Zaletel, and A. Yazdani, Visualizing broken symmetry and topological defects in a quantum hall ferromagnet, *Science* **375**, 321 (2022).
  - [77] A. Coissard, D. Wander, H. Vignaud, A. G. Grushin, C. Repellin, K. Watanabe, T. Taniguchi, F. Gay, C. B. Winkelmann, H. Courtois, H. Sellier, and B. Sacépé, Imaging tunable quantum hall broken-symmetry orders in graphene, *Nature* **605**, 51 (2022).
  - [78] K. P. Nuckolls, R. L. Lee, M. Oh, D. Wong, T. Soejima, J. P. Hong, D. Călugăru, J. Herzog-Arbeitman, B. A. Bernevig, K. Watanabe, T. Taniguchi, N. Regnault, M. P. Zaletel, and A. Yazdani, Quantum textures of the many-body wavefunctions in magic-angle graphene (2023), [arXiv:2303.00024 \[cond-mat.mes-hall\]](#).
  - [79] H. Kim, Y. Choi, Étienne Lantagne-Hurtubise, C. Lewandowski, A. Thomson, L. Kong, H. Zhou, E. Baum, Y. Zhang, L. Holleis, K. Watanabe, T. Taniguchi, A. F. Young, J. Alicea, and S. Nadj-Perge, Imaging inter-valley coherent order in magic-angle twisted trilayer graphene (2023), [arXiv:2304.10586 \[cond-mat.str-el\]](#).
  - [80] B. Nijholt and A. R. Akhmerov, Orbital effect of magnetic field on the majorana phase diagram, *Phys. Rev. B* **93**, 235434 (2016).
  - [81] M. e. Aghaee (Microsoft Quantum), Inas-al hybrid devices passing the topological gap protocol, *Phys. Rev.*



- B **107**, 245423 (2023).
- [82] See the Supplementary Material for details.
  - [83] Y. Li and M. Koshino, Twist-angle dependence of the proximity spin-orbit coupling in graphene on transition-metal dichalcogenides, *Phys. Rev. B* **99**, 075438 (2019).
  - [84] A. David, P. Rakytá, A. Kormányos, and G. Burkard, Induced spin-orbit coupling in twisted graphene-transition metal dichalcogenide heterobilayers: Twistronics meets spintronics, *Phys. Rev. B* **100**, 085412 (2019).
  - [85] T. Naimier, K. Zollner, M. Gmitra, and J. Fabian, Twist-angle dependent proximity induced spin-orbit coupling in graphene/transition metal dichalcogenide heterostructures, *Phys. Rev. B* **104**, 195156 (2021).
  - [86] J. O. Island, X. Cui, C. Lewandowski, J. Y. Khoo, E. M. Spanton, H. Zhou, D. Rhodes, J. C. Hone, T. Taniguchi, K. Watanabe, L. S. Levitov, M. P. Zaletel, and A. F. Young, Spin-orbit-driven band inversion in bilayer graphene by the van der waals proximity effect, *Nature* **571**, 85 (2019).
  - [87] J. Jung, M. Polini, and A. H. MacDonald, Persistent current states in bilayer graphene, *Phys. Rev. B* **91**, 155423 (2015).
  - [88] Z. Dong, M. Davydova, O. Ogunnaike, and L. Levitov, Isospin- and momentum-polarized orders in bilayer graphene, *Phys. Rev. B* **107**, 075108 (2023).
  - [89] J. Liu, A. C. Potter, K. T. Law, and P. A. Lee, Zero-bias peaks in the tunneling conductance of spin-orbit-coupled superconducting wires with and without majorana end-states, *Phys. Rev. Lett.* **109**, 267002 (2012).
  - [90] D. Bagrets and A. Altland, Class  $d$  spectral peak in majorana quantum wires, *Phys. Rev. Lett.* **109**, 227005 (2012).
  - [91] S. Das Sarma and H. Pan, Disorder-induced zero-bias peaks in majorana nanowires, *Phys. Rev. B* **103**, 195158 (2021).
  - [92] C. Moore, T. D. Stanescu, and S. Tewari, Two-terminal charge tunneling: Disentangling majorana zero modes from partially separated andreev bound states in semiconductor-superconductor heterostructures, *Phys. Rev. B* **97**, 165302 (2018).
  - [93] J. Chen, B. D. Woods, P. Yu, M. Hocevar, D. Car, S. R. Plissard, E. P. A. M. Bakkers, T. D. Stanescu, and S. M. Frolov, Ubiquitous non-majorana zero-bias conductance peaks in nanowire devices, *Phys. Rev. Lett.* **123**, 107703 (2019).
  - [94] T. D. Stanescu and S. Tewari, Robust low-energy andreev bound states in semiconductor-superconductor structures: Importance of partial separation of component majorana bound states, *Phys. Rev. B* **100**, 155429 (2019).
  - [95] E. Prada, P. San-Jose, M. W. A. de Moor, A. Geresdi, E. J. H. Lee, J. Klinovaja, D. Loss, J. Nygård, R. Aguado, and L. P. Kouwenhoven, From andreev to majorana bound states in hybrid superconductor-semiconductor nanowires, *Nat. Rev. Phys.* **2**, 575 (2020).
  - [96] A. Haim and A. Stern, Benefits of weak disorder in one-dimensional topological superconductors, *Phys. Rev. Lett.* **122**, 126801 (2019).
  - [97] T. Laeven, B. Nijholt, M. Wimmer, and A. R. Akhmerov, Enhanced proximity effect in zigzag-shaped majorana josephson junctions, *Phys. Rev. Lett.* **125**, 086802 (2020).
  - [98] Y.-M. Xie, D. K. Efetov, and K. T. Law,  $\varphi_0$ -josephson junction in twisted bilayer graphene induced by a valley-polarized state, *Phys. Rev. Res.* **5**, 023029 (2023).
  - [99] J.-X. Hu, Z.-T. Sun, Y.-M. Xie, and K. T. Law, Josephson diode effect induced by valley polarization in twisted bilayer graphene, *Phys. Rev. Lett.* **130**, 266003 (2023).
  - [100] H. Sainz-Cruz, P. A. Pantaleón, V. o. T. Phong, A. Jimeno-Pozo, and F. Guinea, Junctions and superconducting symmetry in twisted bilayer graphene, *Phys. Rev. Lett.* **131**, 016003 (2023).
  - [101] A. Uri, S. Grover, Y. Cao, J. A. Crosse, K. Bagani, D. Rodan-Legrain, Y. Myasoedov, K. Watanabe, T. Taniguchi, P. Moon, M. Koshino, P. Jarillo-Herrero, and E. Zeldov, Mapping the twist-angle disorder and landau levels in magic-angle graphene, *Nature* **581**, 47 (2020).
  - [102] J. H. Wilson, Y. Fu, S. Das Sarma, and J. H. Pixley, Disorder in twisted bilayer graphene, *Phys. Rev. Res.* **2**, 023325 (2020).
  - [103] J. Jung and A. H. MacDonald, Accurate tight-binding models for the  $\pi$  bands of bilayer graphene, *Phys. Rev. B* **89**, 035405 (2014).
  - [104] Z. Wang, D.-K. Ki, J. Y. Khoo, D. Mauro, H. Berger, L. S. Levitov, and A. F. Morpurgo, Origin and magnitude of ‘designer’ spin-orbit interaction in graphene on semiconducting transition metal dichalcogenides, *Phys. Rev. X* **6**, 041020 (2016).
  - [105] B. Yang, M. Lohmann, D. Barroso, I. Liao, Z. Lin, Y. Liu, L. Bartels, K. Watanabe, T. Taniguchi, and J. Shi, Strong electron-hole symmetric rashba spin-orbit coupling in graphene/monolayer transition metal dichalcogenide heterostructures, *Phys. Rev. B* **96**, 041409 (2017).
  - [106] D. Wang, S. Che, G. Cao, R. Lyu, K. Watanabe, T. Taniguchi, C. N. Lau, and M. Bockrath, Quantum hall effect measurement of spin-orbit coupling strengths in ultraclean bilayer graphene/wse<sub>2</sub> heterostructures, *Nano Letters* **19**, 7028 (2019).
  - [107] J. Amann, T. Völkl, T. Rockinger, D. Kochan, K. Watanabe, T. Taniguchi, J. Fabian, D. Weiss, and J. Eroms, Counterintuitive gate dependence of weak antilocalization in bilayer graphene/wse<sub>2</sub> heterostructures, *Phys. Rev. B* **105**, 115425 (2022).
  - [108] M. Gmitra, D. Kochan, P. Högl, and J. Fabian, Trivial and inverted dirac bands and the emergence of quantum spin hall states in graphene on transition-metal dichalcogenides, *Phys. Rev. B* **93**, 155104 (2016).
  - [109] M. Gmitra and J. Fabian, Proximity effects in bilayer graphene on monolayer wse<sub>2</sub>: Field-effect spin valley locking, spin-orbit valve, and spin transistor, *Phys. Rev. Lett.* **119**, 146401 (2017).
  - [110] M. P. Zaletel and J. Y. Khoo, The gate-tunable strong and fragile topology of multilayer-graphene on a transition metal dichalcogenide (2019), [arXiv:1901.01294 \[cond-mat.mes-hall\]](https://arxiv.org/abs/1901.01294).
  - [111] C. W. J. Beenakker, Universal limit of critical-current fluctuations in mesoscopic josephson junctions, *Phys. Rev. Lett.* **67**, 3836 (1991).
  - [112] Y.-M. Xie, K. T. Law, and P. A. Lee, Topological superconductivity in eus/au/superconductor heterostructures, *Phys. Rev. Res.* **3**, 043086 (2021).
  - [113] S. Manna, P. Wei, Y. Xie, K. T. Law, P. A. Lee, and J. S. Moodera, Signature of a pair of majorana zero modes in superconducting gold surface states, *PNAS* **117**, 8775

- (2020).
- [114] J. P. Hong, T. Soejima, and M. P. Zaletel, Detecting symmetry breaking in magic angle graphene using scanning tunneling microscopy, *Phys. Rev. Lett.* **129**, 147001 (2022).

# Supplementary Material for “Gate-defined topological Josephson junctions in Bernal bilayer graphene”

Ying-Ming Xie,<sup>1,2,3</sup> Étienne Lantagne-Hurtubise,<sup>2,3</sup> Andrea F. Young,<sup>4</sup> Stevan Nadj-Perge,<sup>4,3</sup> Jason Alicea,<sup>2,3</sup>

<sup>1</sup>*Department of Physics, Hong Kong University of Science and Technology, Clear Water Bay, Hong Kong, China*

<sup>2</sup>*Department of Physics, California Institute of Technology, Pasadena, California 91125, USA*

<sup>3</sup>*Institute for Quantum Information and Matter, California Institute of Technology, Pasadena CA 91125, USA*

<sup>4</sup>*Department of Physics, University of California at Santa Barbara, Santa Barbara CA 93106, USA*

<sup>5</sup>*T. J. Watson Laboratory of Applied Physics, California Institute of Technology, 1200 East California Boulevard, Pasadena, California 91125, USA*

## I. MINIMAL MODEL FOR BLG AT FINITE DISPLACEMENT FIELDS

The four-band continuum model describing BLG under a perpendicular displacement field  $D$  can be written as

$$h_{\tau}(\mathbf{k}) = \begin{pmatrix} u/2 & v_0\Pi^{\dagger} & -v_4\Pi^{\dagger} & -v_3\Pi \\ v_0\Pi & \Delta' + u/2 & \gamma_1 & -v_4\Pi^{\dagger} \\ -v_4\Pi & \gamma_1 & \Delta' - u/2 & v_0\Pi^{\dagger} \\ -v_3\Pi^{\dagger} & -v_4\Pi & v_0\Pi & -u/2 \end{pmatrix}. \quad (\text{S1})$$

On the left side,  $\tau = \pm 1$  indicates the two valleys  $\pm\mathbf{K} = (\pm\frac{4\pi}{3a}, 0)$ , with  $a$  the lattice constant, and  $\mathbf{k}$  denotes the momentum measured with respect to  $\pm\mathbf{K}$ . On the right side,  $\Pi = (\tau k_x + ik_y)$  specifies the momentum; the basis is  $\psi_{\tau}(\mathbf{k}) = (\psi_{\tau,A1}(\mathbf{k}), \psi_{\tau,B1}(\mathbf{k}), \psi_{\tau,A2}(\mathbf{k}), \psi_{\tau,B2}(\mathbf{k}))$  with  $A, B$  labeling the sublattice degree of freedom and 1, 2 labeling the layer; and  $v_j \equiv \frac{\sqrt{3}}{2}a\gamma_j$ ,  $\gamma_1$ ,  $\Delta'$ , and  $u$  are band-structure parameters. Specifically,  $\gamma_j$ 's encode various hopping processes,  $\Delta'$  is an on-site potential difference resulting from the stacking, and  $u = -d_{\perp}D/\epsilon_{\text{BLG}}$  is the energy difference between the two layers caused by the perpendicular displacement field  $D$  ( $d_{\perp} = 0.33$  nm is the interlayer distance and  $\epsilon_{\text{BLG}} \approx 4.3$  the relative permittivity of BLG.)

Parameters recovering first-principles band structures are given in Ref. 103: intralayer nearest-neighbor hopping is  $\gamma_0 = 2.61$  meV; interlayer hoppings are  $\gamma_1 = 361$  meV,  $\gamma_3 = 283$  meV,  $\gamma_4 = 138$  meV; and the onsite potential difference is  $\Delta' = 15$  meV. In recent experiments, the  $D$  field yielding optimal superconductivity falls in the range of about  $1 \sim 1.3$  V/nm, corresponding to an energy difference  $u \approx 80$ -100 meV [37, 86]. We fix  $u = 100$  meV in our simulations with  $D \neq 0$ . Figure S1 illustrates the BLG band structures at (a) zero and (b) nonzero displacement field.

In the main text, we proposed a minimal model for the valence band that captures the low-energy dispersion for hole-doped BLG near the Fermi energy in the presence of strong displacement fields:

$$h_0(\mathbf{k}) = -\mu + t_a\mathbf{k}^2 + t_c\mathbf{k}^4 + t_b(k_x^3 - 3k_xk_y^2)\tau_z. \quad (\text{S2})$$

To estimate the effective parameters  $t_{a,b,c}$ , we compare the original bands obtained from  $h_{\tau}(\mathbf{k})$  with those fitted by the proposed minimal model  $h_0(\mathbf{k})$ . We find that the

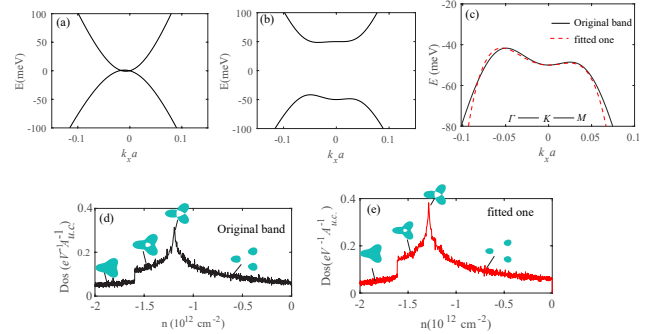


FIG. S1. (a,b) Low-energy bands of BLG in valley  $+\mathbf{K}$  (a) without any displacement field and (b) with a displacement field giving  $u = 100$  meV. (c) Valence-band energy  $E$  versus  $k_x$  in valley  $+\mathbf{K}$  with  $k_y = 0$  and a non-zero displacement field. Solid black line shows the dispersion obtained from the four-band model  $h_+(\mathbf{k})$ , while the dashed red line is a fit using the minimal model  $h_0(\mathbf{k})$ . (d,e) Density of states (Dos) versus hole density obtained from (d) the four-band model and (e) the minimal model, using temperature  $T = 10$  mK for broadening. The insets show the topography of Fermi contours at various hole densities.

dispersions roughly match with  $t_a = 4 \text{ eV} \cdot a^2$ ,  $t_b = -60 \text{ eV} \cdot a^3$ ,  $t_c = -1500 \text{ eV} \cdot a^4$ ; see the energies in Fig. S1(c) as well as the density of states and Fermi contours in Fig. S1(d,e).

## II. SPIN-ORBIT COUPLING IN THE MINIMAL MODEL

At the level of the four-band continuum model, Eq. (S1), the SOC terms appear as [37, 86, 108, 109]

$$h_{\text{SOC},\tau}(\mathbf{k}) = \mathcal{P}_1 \left[ \frac{\lambda_I}{2} \tau s_z + \frac{\lambda_R}{2} (\tau \zeta_x s_y - \zeta_y s_x) \right]. \quad (\text{S3})$$

Here  $\zeta$  and  $s$  are Pauli matrices acting on the sublattice ( $A, B$ ) and spin degree of freedom, respectively, and  $\mathcal{P}_1 = \text{diag}[1, 1, 0, 0]$  projects onto the top layer in the basis used to define Eq. (S1).

Ising and Rashba SOC terms behave very differently within the valence bands of interest. At least for  $\mathbf{k}$  near zero, the BLG valence bands become strongly layer and



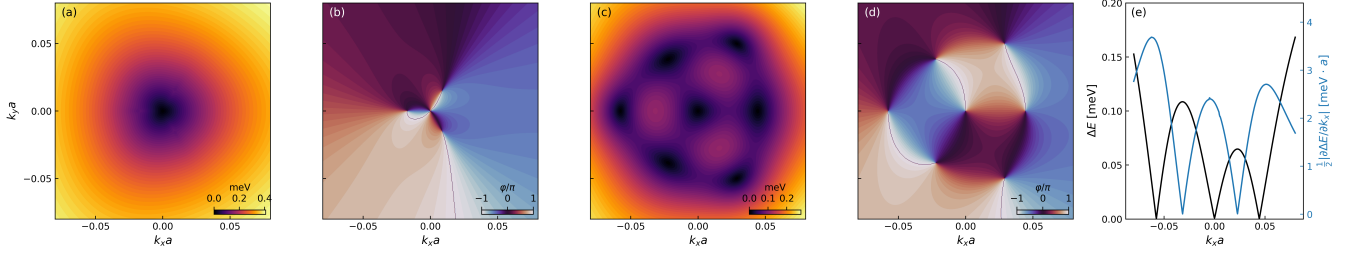


FIG. S2. Rashba SOC effects in the top-most valence band of BLG, in the absence of Ising SOC ( $\lambda_I = 0$ ). We take  $\lambda_R = 1$  meV in Eq. (S3), on the lower end of the experimentally reported range [86, 104–107]. Panels (a,b) correspond to BLG/WSe<sub>2</sub> at zero displacement field  $D$ , while panels (c-e) use  $D \sim 1.3$  V/nm (corresponding to interlayer potential  $u = 100$  meV). The energy difference  $\Delta E$  between the Rashba spin-split valence bands for momenta near the  $\mathbf{K}$  point appears in (a,c); the associated spin winding for the top-most spin-split valence band,  $\varphi \equiv \arg(\langle s_x \rangle + i\langle s_y \rangle)$ , appears in (b,d). (e) Black line: one-dimensional cut through panel (c) for  $k_y = 0$ . Blue dots: derivative of the spin splitting  $\Delta E$  along  $k_x$  (for  $k_y = 0$ ), which gives a proxy for the parameter  $\alpha_R$  defined in the main text [see Eq. (2)].

sublattice polarized by a strong  $D$  field. This polarization negligibly impacts  $\lambda_I$  but suppresses the effects of Rashba SOC due to the latter's off-diagonal structure in sublattice space. Hence, Rashba coupling primarily manifests via virtual excitations to remote bands, which can be understood, e.g., using perturbation theory in the limit where trigonal warping is neglected and one considers a theory with a quadratic band touching at  $D = 0$  (see Ref. 110). In reality, trigonal warping splits the band touching into four Dirac points at  $D = 0$ , around which the spins wind due to Rashba SOC; see Fig. S2(a) and (b). With a strong  $D$  field, the Rashba spin-splitting is suppressed and its texture becomes more complicated; see Fig. S2(c) and (d). The scale of the Rashba spin splitting strongly depends on whether the Fermi surface (in a given valley) comprises three small pockets or a single large pocket. Figure S2(e) shows a one-dimensional cut of the Rashba spin splitting along  $k_x$  with  $k_y = 0$ . As a proxy for the  $\alpha_R$  parameter defined in Eq. (2), (one half of) the derivative of the Rashba spin-splitting as a function of  $k_x$  is shown in Fig. S2(e); note that the spin splitting will be *twice* the energy scale  $\alpha_R k_x$ . In the big Fermi pockets where  $k_x a \sim 0.06$ , we find that a typical scale for  $\alpha_R \sim (1 - 3) \times \lambda_R \cdot a$ . Conservatively estimating  $\lambda_R \sim 1$  meV (on the lower end of the experimentally reported range [86, 104–107]), we then obtain  $\alpha_R \sim 1 - 3$  meV  $\cdot a$ , corresponding to the range specified in the main text.

### III. DETERMINING THE TOPOLOGICAL REGION WITH THE SCATTERING MATRIX METHOD

The solvable toy model for the planar Josephson junction described below Eq. (7) of the main text uses a piecewise-constant valence-band Hamiltonian

$$\tilde{H}_{\text{eff}}(k_x, y) = \frac{\partial_y^2 - k_x^2}{2m} - \mu(y) + \tilde{\alpha}_R(k_x \sigma_y + i \partial_y \sigma_x) + \tilde{h} \sigma_x \quad (\text{S4})$$

with

$$\mu(y) = \mu_1 \theta(L/2 - |y|) + \mu_2 \theta(|y| - L/2). \quad (\text{S5})$$

Above,  $\theta$  is a step function and  $\mu(y)$  captures the chemical potential profile across the device. For the pairing potential we take

$$\Delta(y) = \Delta e^{i \text{sgn}(y) \phi/2} \theta(|y| - L/2). \quad (\text{S6})$$

The phase difference  $\phi$  between the two superconductors can be controlled by applying current or magnetic flux through a loop connected to the junction [63, 64].

The onset of topological superconductivity in the barrier is most easily diagnosed by studying the ABS spectrum at  $k_x = 0$ . For convenience, we rearrange the basis as  $(c_{k_x=0,\uparrow}, c_{k_x=0,\downarrow}, c_{-k_x=0,\downarrow}^\dagger, -c_{-k_x=0,\uparrow}^\dagger)^T$  so that the  $k_x = 0$  BdG Hamiltonian becomes

$$H_{\text{BdG}} = \left[ \frac{\partial_y^2}{2m} - \mu(y) + \tilde{h} \sigma_x \right] \rho_z + i \tilde{\alpha}_R \partial_y \sigma_x \rho_z + \text{Re} \Delta(y) \rho_x + \text{Im} \Delta(y) \rho_y, \quad (\text{S7})$$

where  $\rho$  are Pauli matrices that act in particle-hole space. The analysis is streamlined by the fact that, at  $k_x = 0$ , the BdG Hamiltonian in the preceding basis commutes with  $\eta \equiv \sigma_x$ . In sector  $\eta = \pm 1$ , the Hamiltonian reduces to a  $2 \times 2$  matrix

$$H_\eta = \begin{pmatrix} \xi(y) + i \eta \tilde{\alpha}_R \partial_y + \eta \tilde{h} & \Delta(y) \\ \Delta(y)^* & -\xi(y) - i \eta \tilde{\alpha}_R \partial_y + \eta \tilde{h} \end{pmatrix} \quad (\text{S8})$$

with  $\xi(y) = \partial_y^2/(2m) - \mu(y)$ . Next, we find the ABS energies using scattering matrix formalism.

In the barrier region ( $\Delta = 0$ ,  $\mu = \mu_1$ ), the energies are  $\epsilon = \pm[-k_y^2/(2m) - \mu_1] \pm \eta \tilde{\alpha}_R k_y + \eta \tilde{h}$  with associated

TABLE S1. Classification of possible translation-invariant IVC order parameters, and other types of order parameters for comparison, based on time-reversal  $\mathcal{T}$ ,  $C_3$  rotation, mirror operation  $M_x = i\tau_x s_x$ , and  $U_v(1)$  rotation symmetries.

$\Delta_n$	$\mathcal{T} = i\tau_x s_y K$	$C_3 = e^{-i\frac{\pi}{3}s_z}$	$M_x = i\tau_x s_x$	$U_v(1) = e^{i\varphi\tau_z}$	comment
$\tau_x(s_x, s_y)$	-1	$(x, y)$	$(+1, -1)$	no	nematic IVC
$\tau_y(s_x, s_y)$	-1	$(x, y)$	$(-1, +1)$	no	nematic IVC
$\tau_x s_0$	+1	+1	+1	no	IVC
$\tau_x s_z$	-1	+1	-1	no	spin-valley intertwined IVC
$\tau_y s_0$	+1	+1	-1	no	IVC
$\tau_y s_z$	-1	+1	+1	no	spin-valley intertwined IVC
$\tau_z(s_x, s_y)$	+1	$(x, y)$	$(-1, +1)$	yes	nematic valley polarized
$\tau_z s_0$	-1	+1	-1	yes	valley polarized
$\tau_z s_z$	+1	+1	+1	yes	spin-valley polarized
$\tau_0(s_x, s_y)$	-1	$(x, y)$	$(+1, -1)$	yes	nematic spin-polarized
$\tau_0 s_z$	-1	+1	-1	yes	spin polarized
$(k_x, k_y)\tau_x(s_x, s_y)$	+1	$(x, y) \times (x, y)$	$(-1, +1) \times (+1, -1)$	no	spin-orbit-valley intertwined IVC
$(k_x, k_y)\tau_y(s_x, s_y)$	+1	$(x, y) \times (x, y)$	$(-1, +1) \times (-1, +1)$	no	spin-orbit-valley intertwined IVC
$(k_x, k_y)\tau_y s_z$	+1	$(x, y)$	$(-1, +1)$	no	spin-orbit-valley intertwined IVC
$(k_x, k_y)\tau_x s_z$	+1	$(x, y)$	$(+1, -1)$	no	spin-orbit-valley intertwined IVC

wavefunctions

$$\psi_{e,\eta}^\nu = \begin{pmatrix} 1 \\ 0 \end{pmatrix} e^{ik_{F,e}^\nu y}, \quad (\text{S9})$$

$$\psi_{h,\eta}^\nu = \begin{pmatrix} 0 \\ 1 \end{pmatrix} e^{ik_{F,h}^\nu y}, \quad (\text{S10})$$

where

$$k_{F,e}^\nu = \eta m \tilde{\alpha}_R + \nu \sqrt{m^2 \tilde{\alpha}_R^2 + 2m(\eta \tilde{h} - \epsilon - \mu_1)} \quad (\text{S11})$$

$$k_{F,h}^\nu = \eta m \tilde{\alpha}_R - \nu \sqrt{m^2 \tilde{\alpha}_R^2 - 2m(\eta \tilde{h} - \epsilon + \mu_1)} \quad (\text{S12})$$

and  $\nu = \pm$  labels the right versus left movers.

In the superconducting regions ( $\Delta \neq 0$ ,  $\mu = \mu_2$ ), the wavefunctions are instead

$$\psi_{e,\eta}'^\nu = \frac{1}{\sqrt{2}} \begin{pmatrix} e^{i \text{sgn}(y)\phi/2} \\ e^{-i\gamma} \end{pmatrix} e^{ik_{S,e}^\nu y} \quad (\text{S13})$$

$$\psi_{h,\eta}'^\nu = \frac{1}{\sqrt{2}} \begin{pmatrix} e^{i \text{sgn}(y)\phi/2} \\ e^{i\gamma} \end{pmatrix} e^{ik_{S,h}^\nu y}, \quad (\text{S14})$$

where  $\gamma = \arccos\left(\frac{\epsilon - \eta \tilde{h}}{\Delta}\right)$ ,

$$k_{S,e}^\nu = k_{F,e}^\nu + \frac{i\nu \sqrt{\Delta^2 - (\eta \tilde{h} - \epsilon)^2}}{\sqrt{m^2 \tilde{\alpha}_R^2 + 2m(\eta \tilde{h} - \epsilon - \mu_2)}} \quad (\text{S15})$$

$$k_{S,h}^\nu = k_{F,h}^\nu + \frac{-i\nu \sqrt{\Delta^2 - (\eta \tilde{h} - \epsilon)^2}}{\sqrt{m^2 \tilde{\alpha}_R^2 - 2m(\eta \tilde{h} - \epsilon + \mu_2)}}. \quad (\text{S16})$$

With the above modes, it is straightforward to obtain the scattering matrix according to Refs. 111 and 112. We

first focus on the case with a uniform chemical potential in the junction and superconducting regions, i.e.,  $\mu_1 = \mu_2 = \mu$ . In the Andreev limit  $|\mu| \gg (\Delta, B)$ , the reflection matrices at the left interface  $r_L$  and right interface  $r_R$ , and transmission matrices (left to right as  $t_{RL}$  and right to left as  $t_{LR}$ ) are

$$r_L = \begin{pmatrix} 0 & e^{-i\gamma - i\frac{\phi}{2}} \\ e^{-i\gamma + i\frac{\phi}{2}} & 0 \end{pmatrix}, r_R = \begin{pmatrix} 0 & e^{-i\gamma + i\frac{\phi}{2}} \\ e^{-i\gamma - i\frac{\phi}{2}} & 0 \end{pmatrix}, \quad (\text{S17})$$

$$t_{LR} = \begin{pmatrix} e^{ik_{F,e}^+ L} & 0 \\ 0 & e^{ik_{F,h}^+ L} \end{pmatrix}, t_{RL} = \begin{pmatrix} e^{-ik_{F,e}^- L} & 0 \\ 0 & e^{-ik_{F,h}^- L} \end{pmatrix}. \quad (\text{S18})$$

The ABSs energies  $\epsilon_n$  can be solved from  $\text{Det}[1 - r_L t_{LR} r_R t_{RL}] = 0$ , which gives

$$\cos[2\beta_m L - 2\gamma] = \cos(\phi). \quad (\text{S19})$$

Here,  $\beta_m = \frac{k_{F,e}^+ - k_{F,h}^-}{2} \approx \frac{\eta \tilde{h} - \epsilon}{v_F}$ . The main text Eq. (8) then follows by considering the short-junction limit where the Thouless energy satisfies  $E_T = \frac{\pi v_F}{2L} \gg \Delta, h$ .

Now we examine the case with a chemical potential difference  $\mu_1 \neq \mu_2$ . The transmission matrices  $t_{LR}$  and  $t_{RL}$  keep the same form as above, though the reflection matrices now encode additional normal reflections. The matrix  $r_L$  can be written as

$$r_L = \begin{pmatrix} i r e^{i\theta_0} & \sqrt{1 - r^2} e^{i\theta_0} e^{-i\frac{\phi}{2}} \\ \sqrt{1 - r^2} e^{i\theta_0} e^{i\frac{\phi}{2}} & i r e^{i\theta_0} \end{pmatrix}, \quad (\text{S20})$$

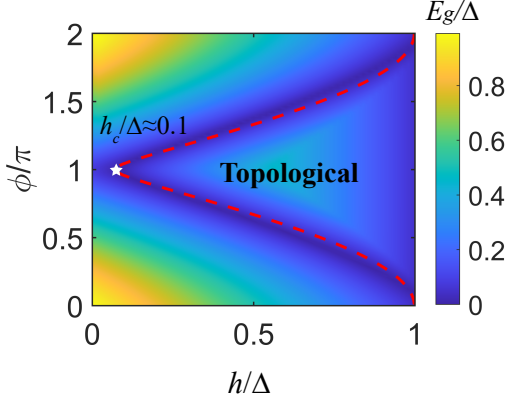


FIG. S3. The  $k_x = 0$  gap  $E_g$  as a function of the Zeeman energy  $h$  and phase difference  $\phi$  calculated from the tight-binding model reviewed in Sec. V. Parameters used are the same as in the main text Fig. 3(c), except that  $\mu_1 = 3$  meV. The red dashed lines are obtained from Eq. (S24) with a normal reflection coefficient  $r = 0.1$ , while the white star indicates the critical field at  $\phi = \pi$  extracted from the tight-binding model.

where

$$re^{i\theta_0} = \frac{2 \sin \gamma (k_1^2 - k_2^2)}{(k_1 + k_2)^2 e^{i\gamma} + (k_1^2 - k_2^2) e^{-i\gamma}}, \quad (\text{S21})$$

$$\sqrt{1 - r^2} e^{i\theta_0} = \frac{4k_1 k_2}{(k_1 + k_2)^2 e^{i\gamma} + (k_1^2 - k_2^2) e^{-i\gamma}}, \quad (\text{S22})$$

and  $k_{1,2} \approx \sqrt{m^2 \tilde{\alpha}_R^2 + 2m|\mu_{1,2}|}$ . If  $\mu_1 = \mu_2$ , one finds that  $r = 0$  and  $\theta_0 = -\gamma$ , thus recovering the preceding results. The reflection matrix  $r_R$  can be obtained by replacing  $\phi \rightarrow -\phi$  in  $r_L$ . One can readily verify unitarity of the reflection matrices  $r_L$  and  $r_R$ .

By solving  $\text{Det}[1 - r_L t_{RL} r_R t_{LR}] = 0$ , we find that ABS energies are determined by

$$\cos(2\theta + 2\beta_m L) + r^2 \cos(2\beta_p L) = (1 - r^2) \cos(\phi). \quad (\text{S23})$$

Here, the average Fermi wavelength between the left-moving and right-moving states reads  $\beta_p = \frac{k_{F,e}^+ - k_{F,e}^-}{2} \approx k_1$ . In the short junction limit with weak normal reflections, we can approximate Eq. (S23) as

$$\cos(2\gamma) = (1 - r^2) \cos(\phi). \quad (\text{S24})$$

Near  $\phi = \pi$ , we can roughly obtain the topological phase transition line as  $\tilde{h}/\Delta = |\cos(\phi/2)| + r/\sqrt{2} \sin(\phi/2)$ .

Let us compare the topological transition line given by Eq. (S24) to our tight-binding model calculation (see Sec. V later), as we have done for the main text Fig. 3(c). In Fig. 3(c), the chemical potential difference between the superconducting and barrier regions does not produce obvious effects. Here, we instead choose  $\mu_1 = 3$  meV,  $\mu_2 = -1$  meV to amplify the role of chemical potential mismatch. In this case, the gap  $E_g$  (extracted from the tight-binding model) as a function of Zeeman energy  $h$

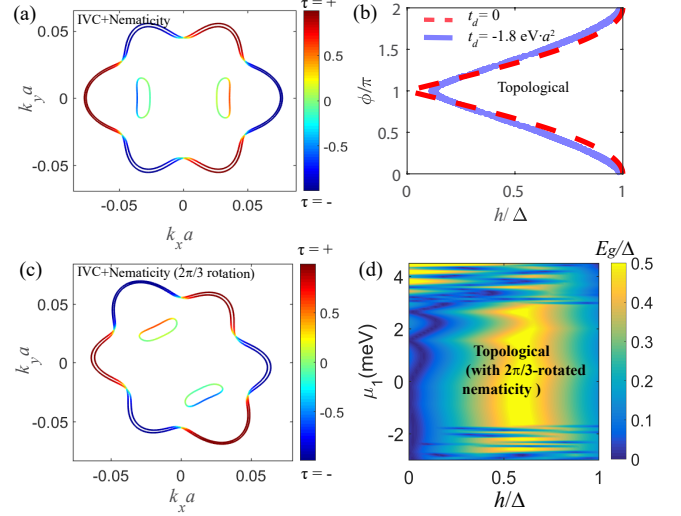


FIG. S4. (a,c) Fermi contours in the presence of finite nematicity modeled with  $t_d = -3$  eV  $\cdot a^2$ . Panel (c) differs from (a) by a  $2\pi/3$  rotation on the nematicity direction. Other parameters are the same as for the main text Fig. 2(c). (b) Topological phase transition lines in the case with nematicity ( $t_d = -1.8$  eV  $\cdot a^2$ ) and without nematicity ( $t_d = 0$ ). Other parameters are the same as for the main text Fig. 3(f). Near  $\phi = \pi$ , the critical magnetic field to enter into the topological regions is modified slightly due to normal reflections enhanced by  $t_d \neq 0$  in this case. (d) Gap  $E_g$  versus  $h$  and  $\mu_1$  obtained assuming the Fermi surface structure from (c). Other parameters are the same as for the main text Fig. 3(d).

and phase difference  $\phi$  is shown in Fig. S3. Note that the effective Zeeman energy felt by the partially occupied bands is weakly renormalized (i.e.,  $\tilde{h} \approx h$ ) when  $\lambda_0 \gg \beta_I$ , as arises here. The red line is calculated from Eq. (S24) with a normal reflection magnitude  $r = 0.1$ , which shows good agreement with the phase transition line indicated by  $E_g$ . The dominant change to the phase diagram occurs near  $\phi = \pi$ , where a finite Zeeman energy of  $r\Delta/\sqrt{2}$  is now needed to drive the junction into the topological phase, contrary to the  $r = 0$  case where arbitrarily weak fields suffice.

#### IV. INCORPORATING NEMATICITY

Experiments [37, 38] suggest that the number of small Fermi pockets present in the superconducting regime may be smaller than six due to nematicity. To phenomenologically incorporate such effects, we explicitly break  $C_3$  symmetry by replacing  $\xi_0(\mathbf{k}) \rightarrow \xi_0(\mathbf{k}) + t_d k_y^2$  in  $h_0(\mathbf{k})$  from the main text. Figure S4(a) illustrates the resulting Fermi contours—which for chemical potential and  $t_d$  value used exhibits only two small pockets. In the range  $t_d \sim -6$  to  $-1.5$  eV  $\cdot a^2$ , the Fermi pockets look similar: large pockets plus two small pockets near  $k_y = 0$ . A smaller  $t_d$  would introduce other small pockets, while a



larger  $t_d$  would dramatically distort the large pockets. We also verified that the chemical potential window at which the Fermi surface hosts only large Fermi pockets is only weakly affected by the introduction of  $t_d$ . The influence of nematicity (modeled in this fashion) on the topological region in the  $h$ - $\phi$  and  $h$ - $\mu_1$  planes appear in Fig. S4(b) and the main text Fig. 3(e), respectively. It can be seen that the nematicity does not appreciably affect the topological region in the  $h$ - $\phi$  plane. However, the robust topological region significantly broadens in the  $h$ - $\mu_1$  plane by removing the small pockets near  $k_x = 0$  through the presence of nematicity.

In the preceding analysis we explicitly specified which two of the six small pockets remained in the presence of nematicity. In principle, one can rotate the nematicity direction so that a different pair of two small pockets appears near Fermi energy. We find that the robust topological regime is mainly hampered by states near zero momentum along the junction (in our setup near  $k_x = 0$ ). In other words, provided the presence of nematicity can remove those states efficiently—which we find holds when the nematicity is strong enough to keep

only two small pockets—the robust topological regime would be enlarged. Figure S4(c) illustrates a different set of two small pockets after a  $2\pi/3$  rotation of the nematicity direction [ $t_d k_y^2 \mapsto t_d (\frac{\sqrt{3}}{2} k_x + \frac{1}{2} k_y)^2$ ] with respect to Fig. S4(a); as seen in Fig. S4(d), in this case a robust topological regime appears for  $\mu_1 \sim (-2, 3)$  meV resembling that in the main text Fig. 3(e).

## V. EFFECTIVE TIGHT-BINDING HAMILTONIAN FOR BLG/WSE2 JOSEPHSON JUNCTION

The tight-binding Hamiltonian used in the main text is deduced from the mean-field Hamiltonian Eq. (7) via a partial Fourier transform along  $y$ -direction. As an illustration, we present the resulting tight-binding Hamiltonian where the  $y$ -direction (perpendicular to the junction) is open while  $k_x$  is still a good quantum number. This tight-binding Hamiltonian can be written as

$$\begin{aligned}
 H_{tb} = \sum_j \left\{ \Psi_{k_x,j}^\dagger \left[ ((t_a + 4t_c)k_x^2 + t_c k_x^4 - \mu_j + E_0) + (t_b k_x^3 - 6t_b k_x) \tau_z + \frac{\beta_I}{2} \tau_z s_z + \alpha_R k_x s_y + \lambda_0 \tau_x + \lambda_1 k_x s_y + h s_x \right] \Psi_{k_x,j} \right. \\
 \left. + \Psi_{k_x,j}^\dagger \left[ -(t_a + t_d + 2t_c k_x^2 + 4t_c) + 3t_b k_x \tau_z - \frac{\alpha_R}{2i} s_x - \frac{\lambda_1}{2i} \tau_x s_x \right] \Psi_{k_x,j+1} + t_c \Psi_{k_x,j}^\dagger \Psi_{k_x,j+2} \right\} \\
 + \sum_{j < -L/2} \Delta e^{i\phi/2} \Psi_{k_x,j}^\dagger (i\tau_x s_y) \Psi_{-k_x,j}^\dagger + \sum_{j > L/2} \Delta e^{-i\phi/2} \Psi_{k_x,j}^\dagger (i\tau_x s_y) \Psi_{-k_x,j}^\dagger + \text{H.c.}
 \end{aligned} \tag{S25}$$

Here,  $j$  labels lattice sites along the  $y$  direction ( $j = 0$  corresponds to the middle of the junction); the four-component annihilation operator is  $\Psi_{k_x,j} = (c_{+\uparrow,j}(k_x), c_{+\downarrow,j}(k_x), c_{-\uparrow,j}(k_x), c_{-\downarrow,j}(k_x))^T$ ; the chemical potential is  $\mu_j = \mu_2 \theta(|j|a - L/2) + \mu_1 \theta(L/2 - |j|a)$ , and  $E_0 = 2(t_a + t_d) + 6t_c$  is a constant energy shift. We have defined the pairing matrix as  $i\tau_x s_y$ , which is an intervalley spin-singlet pairing. After projecting into the low-energy subspace spanned by Pauli matrices  $\sigma_i$ , this pairing takes the form  $i\sigma_y$  as defined in the main text.

A similar calculation using a tight-binding model to simulate the continuum model can be found in Refs. 112 and 113. Figures 3 and 4 of the main text and Figs. (S3 to S7) of the supplemental material are obtained from the above tight-binding model Hamiltonian  $H_{tb}$ . IVC order, when present, is always taken to be position-independent for simplicity, e.g., we assume that it is also present in the barrier of the gate-defined Josephson junction.

## VI. THE MINIMAL TOPOLOGICAL GAP IN VARIOUS PARAMETER REGIONS

Figure S5(a) illustrates the  $k_x$ -dependent ABS spectrum for a topological phase with  $\phi = \pi$  and  $h = 0.8\Delta$ . Notice that the  $k_x = 0$  gap  $E_g$  exceeds the minimal gap  $E_{g,m}$ . The  $E_{g,m}$  gap—which limits the decay length of MZMs in the barrier—typically arises at finite  $k_x$  [Fig. S5(a)] and depends on various model parameters as shown in Fig. S5(b-d). In our simulations the optimal  $E_{g,m}$  approaches  $\sim 0.2\Delta$  and tends to occur (i) over a broad range of lengths ( $L \sim 50 - 200$  nm) in the short-junction regime; (ii) for  $\mu_1 \sim 0 - 3$  meV, where the barrier region is devoid of small Fermi pockets; and (iii) when Rashba coupling energy  $\alpha_R k_F$  is sufficiently large relative to Ising SOC. Requirement (iii) follows from the fact that Ising SOC renormalizes downward the effective Rashba SOC for the relevant large Fermi surfaces; recall Eq. (6) in the main text.

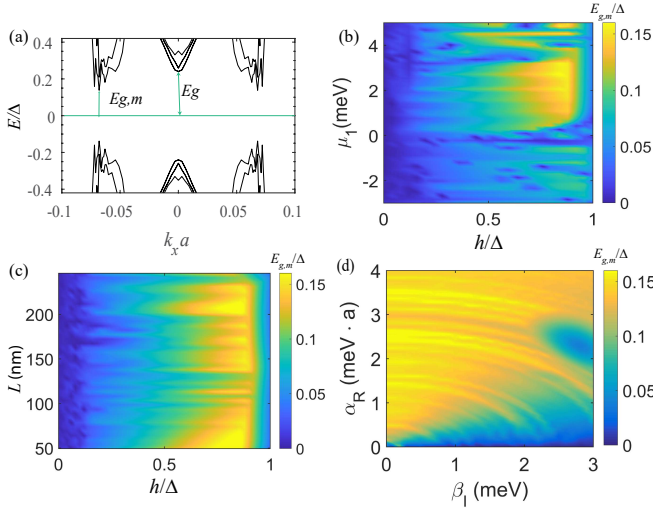


FIG. S5. (a) ABS spectrum versus  $k_x$  obtained from the tight-binding model [Eq. (S25)] with Zeeman field  $h = 0.8\Delta$ . The gap  $E_g$  at  $k_x = 0$  and the minimal gap  $E_{g,m}$  are highlighted. (b-d) Dependence of  $E_{g,m}$  on various junction parameters. Data correspond to  $L = 78$  nm,  $\mu_1 = 2$  meV,  $\mu_2 = -1$  meV,  $\beta_I = 1.4$  meV,  $\alpha_R = 2\text{meV} \cdot a$ ,  $\lambda_0 = 3$  meV,  $\lambda_1 = 0$ ,  $h = 0.8\Delta$ , and  $\phi = \pi$ .

## VII. TUNNELING SPECTROSCOPY AND MAJORANA ZERO-MODES

The topological phase of the BLG/WSe<sub>2</sub> planar Josephson junction hosts a single MZM localized to each end of the barrier. Tunneling constitutes a commonly deployed—though subtle to interpret unambiguously—experimental tool for diagnosing the presence of Majorana modes. Figure S6(a,c) sketches two possible transport experiments to which our setup is amenable: (a) tunneling spectroscopy from a lead directly into the end of the barrier and (c) scanning tunneling microscopy (STM) that probes the full spatial extent of the barrier. The lead in (a) could in principle arise from the BLG/WSe<sub>2</sub> medium itself upon introducing appropriate tunnel barriers via gates; while STM offers a broader spatial field of view, the accessible temperatures are comparatively high, possibly on the scale of or larger than the topological gap for the junction. In this section we examine the LDOS in the barrier—which is expected to roughly track the conductances measured in such tunneling experiments. The LDOS at sites  $\mathbf{r}_j$  is obtained from the Green's functions

$$\rho_{\text{LDOS}}(\mathbf{r}_j) = -\frac{1}{\pi} \text{Im}\{\text{tr}[G(\mathbf{r}_j)]\}. \quad (\text{S26})$$

Here,  $G(\mathbf{r}_j)$  denotes the Green's function at site  $\mathbf{r}_j$ , and the trace is taken over the valley and spin space. The LDOS is evaluated on a discrete grid of positions  $\mathbf{r}_j$  used to define the effective tight-binding model Eq. S25—a discretized version of the low-energy continuum Hamiltonian in the main text. In the next section, we will show

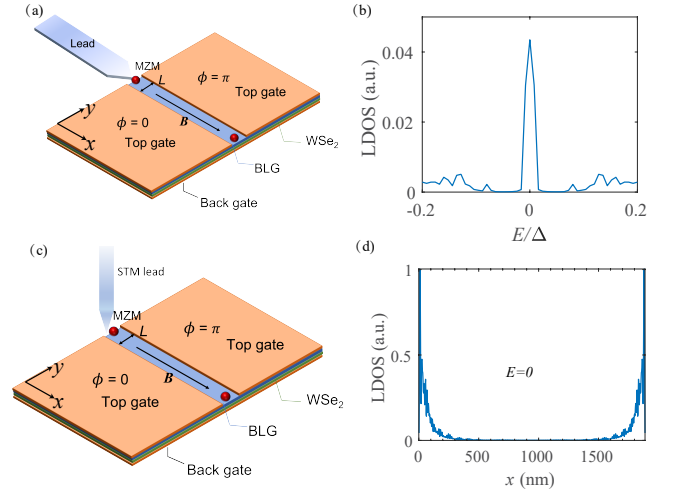


FIG. S6. (a,c) Illustration of detection schemes for Majorana zero-energy modes (MZMs) in the BLG/WSe<sub>2</sub> planar Josephson junction. (b,d) Local density of states (LDOS) that roughly mimics the conductance measured in the setups from (a,c). Panel (b) shows the energy dependence of the LDOS near the end of the barrier in the topological phase of the Josephson junction. The zero-bias peak originates from the MZM localized at the boundary. Panel (d) shows the position dependence of the zero-energy LDOS within the barrier—which maps the spatial structure of the Majorana modes. Data in (b,d) were obtained assuming the following:  $L = 50$  nm,  $\mu_1 = 2$  meV,  $\mu_2 = -1$  meV,  $\beta_I = 1.4$  meV,  $\alpha_R = 2\text{meV} \cdot a$ ,  $\lambda_0 = 3$  meV,  $\lambda_1 = 0$ ,  $h = 0.8\Delta$ ,  $\phi = \pi$ , and broadening parameter  $\eta = i\Delta/1000$ .

how to recover the full atomically resolved LDOS by introducing Wannier functions to describe atomic orbitals.

We obtain the LDOS from our tight-binding model [Eq. (S25)] by Fourier also transforming along the  $x$  direction, taking open boundary conditions to introduce endpoints for the barrier, and using the lattice Green's function method [112, 113] to obtain the Green's function  $G_{nn}(E) = (E - H_{nn} - \Sigma + i\eta)^{-1}$  of the column representing the middle of the junction region, i.e.,  $y = 0$ , where  $H_{nn}$  is the Hamiltonian of  $n$ -th column,  $\Sigma$  is the self-energy due to the coupling between nearest columns, and  $\eta$  is a broadening parameter. See the caption of Fig. S6 for parameters. Figure S6(b) presents the energy dependence of the LDOS evaluated near the end of the barrier. The pronounced zero-bias peak reflects the associated localized MZM, and is the counterpart of the (quantized) zero-bias peak that would arise at zero temperature in the transport setup from panel (a). Figure S6(d) shows the spatial profile of the LDOS at zero energy, which is relevant for the STM setup from panel (b). Well-localized MZM wavefunctions—one from each end—are clearly visible; with the (not unreasonable) parameters used here, the decay length is on the 100 nm scale.

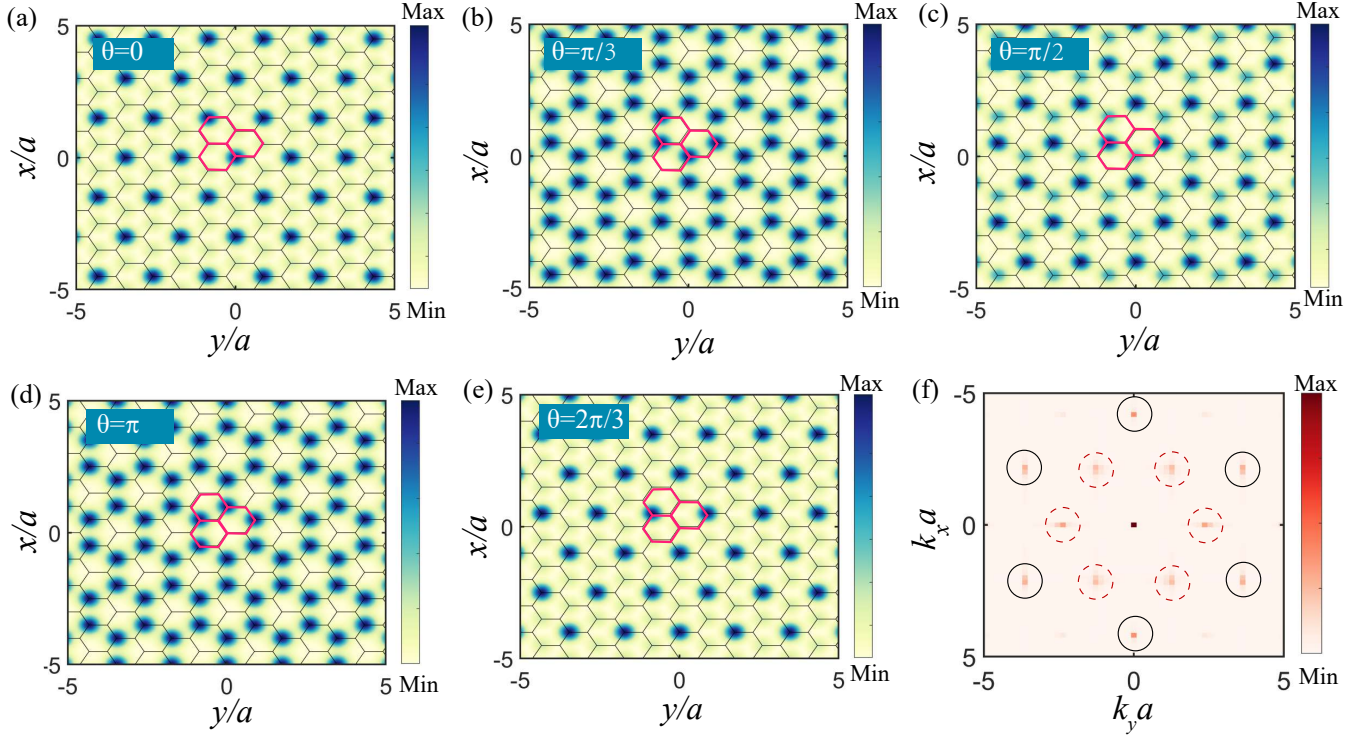


FIG. S7. (a-e) Kekulé patterns obtained from extended bulk states with energy  $E = 1.2\Delta$  at various Kekulé angles  $\theta$ . Three graphene hexagonal plaquettes are highlighted in pink color, which forms a Kekulé supercell. Note that mirror symmetry  $M_x$  is preserved only for  $\theta = 0$  and  $\pi$  which correspond to a  $\tau_x$  IVC order parameter (see SM Table S1). (f) Fourier transform of data in (a) for  $\theta = 0$  (other angles exhibit similar features). Kekulé peaks are highlighted with red dashed circles.

### VIII. COMPUTING ATOMICALLY RESOLVED MAJORANA ZERO MODE WAVEFUNCTIONS

The formalism of the previous section allows us to evaluate a ‘coarse-grained’ version of the LDOS, which captures the broad features of the low-energy wavefunctions but disregards atomically resolved information. We can capture the finer, atomic-scale structure of the LDOS by invoking Wannier functions that describe the relevant atomic orbitals. As shown in the main text, the necessity of IVC order to obtain topological superconductivity in our setup endows MZM wavefunctions with atomic-scale fingerprints, potentially detectable via STM. In this section, we explain the method used to compute those atomically resolved MZM wavefunctions.

For the purposes of this section, we parametrize the (spin-unpolarized) IVC order parameter as

$$\Delta_{\text{IVC}} = \cos(\theta)\tau_x + \sin(\theta)\tau_y, \quad (\text{S27})$$

where  $\theta$  denotes the Kekulé angle. Except for Fig. 4 of the main text, a  $\tau_x$  order parameter (which respects the mirror symmetry  $M_x$ ) was assumed, corresponding to  $\theta = 0$ . Different values of  $\theta$  are contrasted in Fig. 4 to aid with experimental identification of IVC orders.

The LDOS, now including atomic-scale structure, is

given by

$$\rho(E, \mathbf{r}) = -\frac{1}{\pi} \text{Im} \sum_n \frac{|\psi_n(\mathbf{r})|^2}{E - E_n + i\eta} \quad (\text{S28})$$

where  $\eta > 0$  is a small broadening parameter and  $\psi_n(\mathbf{r})$  is the wavefunction for an eigenstate with energy  $E_n$  in the  $n$ -th band,

$$\psi_n(\mathbf{r}) = \sum_{\mathbf{r}_\alpha, \tau, s} c_{n, \tau, s}(\mathbf{r}_\alpha) e^{i\mathbf{K}_\tau \cdot \mathbf{r}_\alpha} \phi_\alpha(\mathbf{r} - \mathbf{r}_\alpha). \quad (\text{S29})$$

Here  $\tau, s$  respectively denote valley and spin indices,  $\mathbf{K}_\tau = (\tau 4\pi/3a, 0)$ , and  $\phi_\alpha(\mathbf{r} - \mathbf{r}_\alpha)$  represent localized Wannier wavefunctions at lattice site  $\mathbf{r}_\alpha$ . The coefficients  $c_{n, \tau, s}$  can be obtained from diagonalizing the tight-binding Hamiltonian in Eq. (S25) with the IVC order parameter now given by Eq. (S27). For bulk states,  $c_{n, \tau, s}$  are expected to be uniform in real space, while for MZMs in a junction geometry they display an exponential decay with localization length  $\xi$ .

Substituting Eq. (S29) into Eq. (S28), the LDOS can be decomposed into two contributions:  $\rho(E, \mathbf{r}) = \rho_0(E, \mathbf{r}) + \delta\rho(E, \mathbf{r})$ . The first piece,

$$\rho_0(E, \mathbf{r}) = -\frac{1}{\pi} \text{Im} \sum_{\tau\tau', \mathbf{r}_\alpha} \text{tr}[G_{\tau\tau'}(\mathbf{r}_\alpha, \mathbf{r}_\alpha)] \times e^{i(\mathbf{K}_\tau - \mathbf{K}_{\tau'}) \cdot \mathbf{r}_\alpha} |\phi(\mathbf{r} - \mathbf{r}_\alpha)|^2, \quad (\text{S30})$$



involves Wannier orbitals at the same lattice site  $\mathbf{r}_\alpha$ , while the second,  $\delta\rho(E, \mathbf{r})$ , includes all contributions with Wannier orbitals evaluated at different lattice sites. In the equation above,  $G_{\tau\tau'}(\mathbf{r}_\alpha, \mathbf{r}_\alpha)$  is a Green's function (the spin indices are omitted for simplicity) that can be directly calculated from the tight-binding Hamiltonian, Eq. (S25), using the recursive Green's function method [112, 113]. Since the relevant wavefunctions at the large  $D$  fields of interest are well-localized on one layer, and on one sublattice, the contribution from  $\delta\rho(E, \mathbf{r})$  is expected to be significantly suppressed compared to  $\rho_0(E, \mathbf{r})$ ; moreover,  $\rho_0(E, \mathbf{r})$  already suffices to capture atomic-scale structure descending from IVC order. We therefore neglect  $\delta\rho(E, \mathbf{r})$  hereafter.

To model the atomic orbitals, we consider Gaussian Wannier functions [79, 114]:

$$\phi(\mathbf{r} - \mathbf{r}_\alpha) = \frac{1}{\sqrt{2\pi}} e^{-\frac{(\mathbf{r} - \mathbf{r}_\alpha)^2}{2\sigma^2}}. \quad (\text{S31})$$

In our simulations, we take  $\sigma = 0.3a$ . Using this choice, the contribution  $\delta\rho$  is indeed unimportant. Due to the large displacement field  $D$ , we expect the valence-band wavefunctions will be pushed onto the  $B_2$  sites (or the

$A_1$  sites for the opposite sign of the displacement field). Therefore, we position the Wannier centers of our tight-binding model on the  $B_2$  sites, forming a triangular lattice.

As an illustration, Fig. S7(a-e) plots the atomically resolved wavefunction of extended bulk states with energy  $E = 1.2\Delta$ , for various Kekulé angles  $\theta$ . Unlike the Kekulé pattern for MZMs presented in the main text, here the patterns are translationally invariant—albeit with an enlarged unit cell reflecting IVC order. The main text Figs. 4(c-e) can thus be understood as a uniform Kekulé pattern at the corresponding Kekulé angle, superimposed on the additional spatial modulations coming from the exponentially decaying spatial profile of MZMs. There is a small asymmetry between the LDOS at  $y$  and  $-y$  in the main text Figs. 4(c-e) arising from explicit breaking of mirror symmetry  $M_y$  in the low-energy theory. This breaking is manifest in the second term of Eq. (5), which arises from a combination of Ising SOC and trigonal warping. Figure S7(f) illustrates that, by similarly Fourier transforming the extended Kekulé bulk states, we obtain the usual Kekulé peaks in momentum space.